EXTENDED AND FINITE GRAPHENES: COMPUTATIONAL STUDIES OF MAGNETIC RESONANCE AND MAGNETO-OPTIC PROPERTIES

JARKKO VÄHÄKANGAS

NMR Research Group
University of Oulu
Finland

Academic dissertation to be presented with the assent of the Doctoral Training Committee of Technology and Natural Sciences of the University of Oulu for public discussion in the Auditorium L10, Linnanmaa, on August 20$^{\text{th}}$ 2015, at 12 o'clock noon.

REPORT SERIES IN PHYSICAL SCIENCES Report No. 97
OULU 2015 • UNIVERSITY OF OULU

Opponent
Professor Oleg Yazyev
Ecole Polytechnique Fédérale de Lausanne (EPFL), Switzerland

Reviewers
Assistant Professor Chiara Cappelli
Università di Pisa, Italy

Assistant Professor Antti Karttunen
Aalto University, Finland

Custos
Professor Juha Vaara
University of Oulu, Finland

ISBN 978-951-42-0860-2 (Paperback)
ISBN 978-952-62-0861-9 (PDF)
ISSN 1239-4327
Juvenes print Oulu 2015

Vähäkangas, Jarkko: **Extended and Finite Graphenes: Computational Studies of Magnetic Resonance and Magneto-Optic Properties, University of Oulu, P.O.Box 3000, FIN-90014 University of Oulu, Finland**
Report Series in Physical Sciences No. 97 (2015)

Abstract

In this thesis, the magnetic resonance and magneto-optical rotation parameters are studied in single-layer carbon systems of two different dimensionalities. Based on electronic structure calculations, the spectral parameters are predicted for both extended (2D) and finite, molecular (0D) systems consisting of pure sp^2-hybridised pristine graphene (G), as well as hydrogenated and fluorinated, sp^3-hybridised graphene derivatives, graphane (HG) and fluorographene (FG), respectively.

Nuclear magnetic resonance (NMR) parameters are calculated for G, HG and FG systems at their large-system limit. For their 0D counterparts, graphene flakes, qualitative spectral trends are predicted as functions of their size and perimeter type. The last group of studied carbon systems consists of 2D graphenes containing spin-1/2 paramagnetic defects. Electron spin resonance (ESR) parameters and paramagnetic NMR shieldings are predicted for four different paramagnetic systems, including the vacancy-defected graphane and fluorographene, as well as graphene with hydrogen and fluorine adatoms. The magneto-optic properties of G and HG flakes are studied in terms of Faraday optical rotation and nuclear spin optical rotation parameters, to investigate the effects of their finite size and also the different level of hydrogenation.

All the different investigated parameters displayed characteristic sensitivity to the electronic and atomic structure of the studied graphenes. The parameters obtained provide an insight into the physics of these 0D and 2D carbon materials, and encourage experimental verification.

Keywords: graphene, graphane, fluorographene, nuclear magnetic resonance, electron spin resonance, Faraday effect, nuclear spin optical rotation, spectral parameters, electronic structure, density-functional theory

To Maria
and our lovely children
Sulo and Alma

Acknowledgements

First of all, I would like to thank my supervisors, Prof. Juha Vaara and Dr. Perttu Lantto. This thesis is the result of your teaching and guidance to do research with your high-level scientific knowledge and excellent mentoring. Juha, your enthusiasm for science, your personality, and good leadership skills have a great influence on the existing supportive and active atmosphere in the NMR research group. Despite your occasionally tight schedule you always found time to answer my "short questions" and commented on manuscripts with elaboration. Perttu, I respect your availability and unlimited patience as well as expertise on practical computing-related issues, which were a determining factor for the successful completion of the work presented in this thesis.

Furthermore, I would like to thank the reviewers of this thesis, Dr. Chiara Cappelli and Dr. Antti Karttunen for their work and valuable comments. Co-authors Suvi Ikäläinen, Nergiz Özcan-Ketola, and Jiří Mareš are also warmly appreciated.

From the University of Oulu, I would like to thank Prof. Matti Weckström for placing the facilities at my disposal. The work was financially supported by the Vilho, Yrjö and Kalle Väisälä Foundation, the Department of Physics, Oulu University Scholarship Foundation, the Tauno Tönning Foundation, and the University of Oulu Graduate School. The Finnish IT Center for Science (CSC) provided most of the computational resources.

I am grateful for the opportinity to share the office with a colleague like you, Juho. In addition to taking advantage of your computer skills uncountable times, our daily discussions on physics as well as non-scientific conversations were very important to me. Thanks also for showing me an exemplary attitude towards the study and research. Jiří, thanks for being my colleague and my friend, too. I appreciate your skills of listening to other people and your modest attitude. My thanks also go to the rest of the NMR group members for their supportive and friendly team spirit.

Finally, I would like to thank my family and in-laws for their words of encouragement as well as all the practical help received during all these busy years. Sulo and Alma, you provided me with the essential counterbalance to the work and study. Your vitality and ongoing learning of new skills have inspired me a lot. My beloved wife Maria deserves the most special thanks. Maria, it was your continuous support and heroic efforts that made the completion of this thesis possible.

Oulu, June 2015 Jarkko Vähäkangas

List of original papers

The present thesis consists of an introductory part and the following original papers, which are referred to in the text by their Roman numerals:

I J. Vähäkangas, S. Ikäläinen, P. Lantto, and J. Vaara
Nuclear Magnetic Resonance Predictions for Graphenes: Concentric Finite Models and Extrapolation to Large Systems.
Phys. Chem. Chem. Phys. **15**, 4634 (2013).

II N. Özcan, J. Vähäkangas, P. Lantto, and J. Vaara
Characteristic Spectral Patterns in the ^{13}C Nuclear Magnetic Resonance of Hexagonal and Crenellated Graphene Fragments.
ChemPhysChem **15**, 1799 (2014).

III J. Vähäkangas, P. Lantto, J. Mareš, and J. Vaara
Spin Doublet Point Defects in Graphenes: Predictions for ESR and pNMR Spectral Parameters.
Manuscript submitted for publication.

IV J. Vähäkangas, P. Lantto, and J. Vaara
Faraday Rotation in Graphene Quantum Dots: Interplay of Size, Perimeter Type and Functionalization.
J. Phys. Chem. C **118**, 23996 (2014).

The author has participated in the planning of all the studies and carried out all the quantum-chemical calculations as well as the analysis of the data in Papers I, III and IV, as well as partially those of Paper II. Furthermore, the first versions of the manuscripts of Papers I, III and IV were written by the author. All articles were finished as teamwork.

Abbreviations

B3LYP	Becke 3-parameter exchange functional plus Lee-Yang-Parr correlation functional
BHandHLYP	hybrid functional with half Becke exchange and half Hartree-Fock exchange, as well as LYP correlation part
co	completeness-optimised (basis set)
DFT	density-functional theory
DSO	diamagnetic nuclear spin-electron orbit (operator, contribution)
EFG	electric field gradient
ESR	electron spin resonance
FC	Fermi contact (operator, contribution)
FG	fluorographene (fluorinated graphene)
FOR	Faraday optical rotation
GGA	generalised gradient approximation
GIAO	gauge-including atomic orbital
GIPAW	gauge-including projector augmented wave
G	graphene
GQD	graphene quantum dot
GTO	Gaussian-type orbital
HF	Hartree-Fock
HG	graphane (hydrogenated graphene)
HFC	hyperfine coupling (tensor)
KS	Kohn-Sham (orbital, equation, reference state)
LCAO	linear combination of atomic orbitals
LDA	local density approximation
LPL	linearly polarised light
LYP	Lee-Yang-Parr (correlation functional)
LRF	linear response function

NMR	nuclear magnetic resonance
NR	nonrelativistic
NSOR	nuclear spin optical rotation
OZ	orbital Zeeman
PBE	Perdew-Burke-Ernzerhof (GGA functional)
pNMR	paramagnetic NMR
PAW	projector-augmented wave
PSO	paramagnetic nuclear spin-electron orbit (operator, contribution)
SCF	self-consistent field
SD	spin-dipole (operator, contribution)
SO	spin-orbit (operator)
SOO	spin-other-orbit (operator)

Contents

1 Introduction

1.1 Graphenes

Graphene is a two-dimensional allotrope of carbon, where sp^2-hybridised atoms are covalently bonded to three other carbons, forming a honeycomb lattice with the thickness of a single atomic layer. Graphene was presumed to be thermodynamically unstable in its pristine form [1]. Consequently, until the 21st century it was only considered a prototypic, theoretical [2] building block of the rich polymorphism existed by the various other sp^2-hybridised allotropes of carbon, such as the one-dimensional nanotubes and the three-dimensional graphite [3–5]. In 2004, Geim and co-workers managed for the first time to isolate graphene from graphite by mechanical exfoliation [6]. Since then, graphene has fascinated scientists with its unusual electric, optical and mechanical properties, providing a versatile platform for both fundamental and applied research.

By chemically functionalising graphene it is possible to produce derivatives that have different physical properties, such as electrical conductivity and light absorption. The first kind of derivatives were hydrogenated and fluorinated graphenes, called graphane and fluorographene, respectively [7–9]. The attachment of these atoms, hydrogen or fluorine, below and above the sp^2-hybridised carbon layer in an alternating manner changes the hybridisation type to sp^3, preserving the 2D hexagonal symmetery. This induces opening of the vanishing band gap of graphene, resulting these graphene derivatives to be insulators [10]. The atomic structures and electronic band structures of these systems are illustrated in Figrure 1.1.

Large polycyclic and aromatic hydrocarbons (PAHs) can be regarded as finite zero-dimensional graphene flakes. In addition to the fact that they have many of the excellent characteristics of graphene, PAHs also have size-tunable properties [11–14]. From the modelling point-of-view, the innermost part of these sp^2-hybridised flakes possesses a graphene-like environment, which can be used to calculate local molecular properties, such as many magnetic resonance parameters, to extrapolate to the large-system limit.

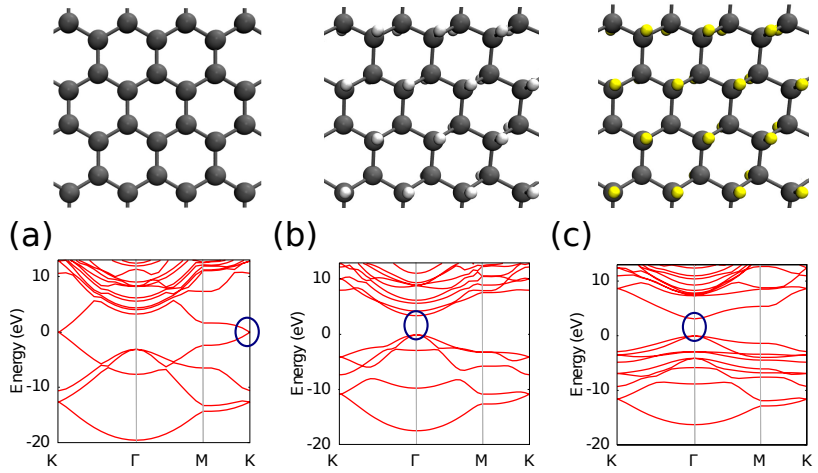

Figure 1.1. Hexagonal atomic structures and electronic band structures of 2D graphenes. Planar (a) sp^2-hybridised graphene as well as (b) hydrogenated (graphane) and (c) fluorinated (fluorographene) sp^3-hybridised systems, the latter two in the chair conformation. The transformation from the sp^2-hybridisation to sp^3 opens the zero band gap of graphene at the K point, resulting in the graphene derivatives possessing a minimal direct gap at the Γ point with the value of a couple of eV, indicated with the blue circles.

1.2 NMR, ESR and pNMR spectroscopies

Most spectroscopic methods are based on the application of the electromagnetic radiation onto the sample and measuring the scattering or absorption of the radiation after its interaction with matter [15]. These experimental techniques have given access to the electronic and atomic structure of matter. Spectra with a plethora of details of the interactions occurring in the target, are obtained when matter responds to the applied electromagnetic perturbation.

Nuclear magnetic resonance (NMR) is a widely used spectroscopic tool not only to characterise sensitively the molecular structures in chemistry, but it is also used in many other scientific disciplines, such as medicine, biology, geology and materials science [16, 17]. The method is based on the NMR-active nuclei, which behave as minuscule magnets due to the non-zero value of their spin quantum number I. The applied external magnetic field forces the macroscopic ensamble of these spins to be aligned with the field. Typically of Nature in a very small scale, the orientation of these nuclei are associated with certain stationary energy states, which in this case result from the interaction with the external magnetic field. Photons introduced by means of radio-frequency pulses can induce transitions between the nuclear spin states. The photons that have exactly the required excitation energy can give rise to resonance. The magnetisation of the excited system relaxes with a characteristic time scale by emitting photons that are received with the detection coil of the NMR instrument. The energy distribution of the photons

gives information of the local electronic and atomic structure of matter, giving spectra characteristic to the environment in all states of matter. This specific information is due to the electronic currents that are induced to the molecule by the applied magnetic field. Furthermore, these currents depend on the electronic structure near the NMR nucleus of interest, resulting in a specific strength of the local magnetic field. This, in turn, is seen as spectral parameters specific to the chemical environmental.

Not only certain nuclei but also the electron cloud of the system can have a magnetic character, due to unpaired electrons that have a much larger magnetic moment than that of any nucleus. For instance, the presence of a metal ion or a lattice defect may cause a paramagnetic center to appear in the material. A spectroscopy method that gives insight to the atomic and electronic structure of material defects is electron spin resonance (ESR) [18, 19]. It shares many principles with NMR but, instead of nuclear spins, ESR deals with the spins of the unpaired electrons. Also the NMR technique can be used to gain structural and dynamical information from paramagnetic systems with unpaired electrons. The so-called paramagnetic NMR (pNMR) is used in the development of new magnetic materials and biomolecular applications, $e.g.$, in the study of metalloproteins [20]. Traditionally pNMR is used when the information obtained by ESR is scarce [21].

Faraday optical rotation (FOR) is a magneto-optic phenomenon, in which the plane of polarisation of a linearly polarised light (LPL) beam rotates when it travels through a material that is exposed to an externally applied magnetic field directed along of the beam [22]. It is the different indices of refraction for the left- and right-circularly polarised light components that results in this optical rotation. The phenomenon can also be used for spectroscopic purposes, because the rotation is dependent on the chemical composition of the molecules in the medium [23]. Recently this phenomenon has been observed as caused by, instead of the external magnetic field, the field that arises from an ensemble of polarised nuclear spins. This effect is dubbed as nuclear spin optical rotation (NSOR) [24, 25]. It offers a novel way to gain information of, in principle, atomic resolution, due to the fact that nuclei in different chemical environments have their characteristic NSOR constants. NSOR has the potential to offer a high-resolution experimental spectroscopic tool, but the applications of NSOR are still in their early infancy.

This dissertation focuses on spectroscopic investigations of different kinds of graphenes (finite and extended; pristine and chemically modified) by means of the above-described magnetic and magneto-optic phenomena. The research has been performed by computational methods. In general, computational science has emerged as a significant methodology in many scientific disciplines. In chemistry and physics, atomic-scale modelling provides valuable insight into the properties of atomic, molecular, and materials systems, in a way that might be unfeasible for experimental techniques. In the field of spectroscopy, computations are widely used to interpret experimental spectra, which often are very rich in detail. The fundamental theory behind these kinds of calculation is quantum mechanics, which revolutionised physics in the early 20th century. Quantum mechanics describes nature with astonishing accuracy in the very small scale, covering fields as distinct as elementary particles to molecules and materials. The present electronic structure calculations belong to the class of first-principles methods, which rely only on controlled approximations, in solving the many-body Schrödinger equation.

1.3 Outline of the dissertation

This dissertation consists of four scientific publications. Papers I and II concern the NMR properties of diamagnetic, $i.e.$, electronically closed-shell graphene systems. In Paper I, the NMR parameters are predicted for extended graphenes obtained by two different computational approaches. Quantum-chemical calculations of concentric, finite models of graphene, graphane and fluorographene, were used to extrapolate the NMR shielding and spin-spin coupling parameters to the large-system limit. These values are compared to the results obtained of solid-state calculations, which deal, due to the periodic boundary conditions used, directly with infinite systems. Paper II concerns, in turn, specifically the finite graphene flakes using quantum-chemical methods. It predicts characteristic carbon-13 NMR chemical shift spectra for increasing-size hexagonal graphene and its hydrogenated and fluorinated derivatives, with different types of boundary structure. The combined results of these two papers provide aid for future NMR analysis of both extended graphenic meterials, as well as different graphene nanoflakes.

Paper III tackles the spin-half paramagnetism that has been predicted and recently also experimentally verified [26] to occur when an adatom is absorbed onto the graphene surface. The ESR g-tensor and the hyperfine coupling tensors, as well as the pNMR shielding tensor obtained by periodic calculations, are reported for the defected, sp^2-hybridised graphene that hosts either hydrogen or fluorine adatoms. Correspondingly, the sp^3-hybridised graphane and fluorographene defected by a hydrogen or a fluorine vacancy, were subjected to a similar inspection. The vacancy defects in the graphane and fluorographene systems constitute sp^2-centers, where the magnetic resonance parameters are locally strongly enhanced. In contrast, adatom-induced magnetic resonance parameters that decay slowly with the distance from the defect, are found in pure graphene, which illustrates the long-ranged perturbation caused by the defect to the electronic structure.

Paper IV presents a study of the magneto-optic properties, specifically Faraday optical rotation and nuclear spin optical rotation, for finite graphene flakes. Systems with different size, perimeter structure and composition are studied in terms of the Verdet and NSOR constants. It is found that, while FOR is independent of the two types of the studied edge geometries, this property shows a characteristic transfer of strong enhancement toward longer wavelengths, as a function of growing system size. Furthermore, FOR is found to be very sensitive to the degree of the sp^2-hybridization, $i.e.$, the fraction of graphene-like area in mixed, sp^3/sp^2-hybridised systems. NSOR provides a means of distinguishing graphene systems of different sizes and different terminations. The study confirms that strong optical activity of the graphene flakes takes place in the visible spectral range.

In addition to this introduction, the dissertation consists of four parts. Chapter 2 describes the main concepts of the used spectroscopies and the underlying physical phenomena. Chapter 3 begins by describing the basic theory of the electronic structure calculation methods used. Furthermore, the chapter focuses on the methods of perturbation theory that enable obtaining the spectroscopy parameters of interest. Chapter 4 reviews the individual Papers included in the dissertation. A summary presented in Chapter 5 closes the thesis.

2 Concepts

2.1 Nuclear magnetic resonance

NMR spectroscopy is based on the characteristic transitions between the stationary spin eigenstates, $i.e.$, Zeeman levels, of nuclei in the presence of an external magnetic field $\mathbf{B}_0$ induced by NMR apparatus [16]. In order to observe these transitions, the sample has to contain, NMR-active, paramagnetic nuclei that possess the spin quantum number $I \geq 1/2$. Such a nucleus has then a magnetic moment, $\mathbf{m}_K = \gamma_K \hbar \mathbf{I}_K$, where γ_K is the gyromagnetic ratio that is determined by the specific nuclear structure and $\mathbf{I}_K$ is the nuclear spin angular momentum. The details of NMR spectra are determined by the microscopic interactions of these magnetic moments, determined by the immediate electronic neighbourhood of the nuclei [16, 17].

An effective nuclear spin Hamiltonian [27] reproduces the observed NMR spectra with the aid of specific parameters, without the explicit consideration of electrons. In such a Hamiltonian, all the other degrees of freedom but nuclear spins are embedded into the spectral parameters, generally expressed as two-index tensors*, $\boldsymbol{\sigma}_K$, $\mathbf{D}_{KL}$, $\mathbf{J}_{KL}$, and $\boldsymbol{\mathcal{B}}_K$. In frequency units ($E/h$) the NMR Hamiltonian is expressed as

$$\begin{aligned} H_{\text{NMR}} = &- \frac{1}{2\pi} \sum_K \gamma_K \mathbf{I}_K \cdot (\mathbf{1} - \boldsymbol{\sigma}_K) \cdot \mathbf{B}_0 + \sum_{K<L} \mathbf{I}_K \cdot (\mathbf{D}_{KL} + \mathbf{J}_{KL}) \cdot \mathbf{I}_L \\ &+ \sum_K \mathbf{I}_K \cdot \boldsymbol{\mathcal{B}}_K \cdot \mathbf{I}_K. \end{aligned} \tag{2.1}$$

The first term in H_{NMR} involves the shielding tensor $\boldsymbol{\sigma}_K$ that parametrises the change to the interaction of the bare nuclear magnetic moment with the external magnetic flux density, $-\boldsymbol{\mu}_K \cdot \mathbf{B}_0$, at the site of the nucleus. This change arises from the electronic environment and its modifications by the magnetic field, which create a secondary, induced magnetic field $\mathbf{B}_K^{\text{ind}}$ at the nuclear site. According to Lenz's law [29] this field (most often)

*A two-index tensor can be represented as a 3×3 matrix, which can be decomposed as a sum of three contributions of tensorial ranks 0, 1 and 2. Rank-0 corresponds to a scalar, rank-1 to an antisymmetric tensor containing three distinct components, and rank-2 to a symmetric tensor having five independent components with zero trace [28].

opposes the external field, as parametrised by the shielding tensor:

$$\mathbf{B}_K^{\text{ind}} = -\boldsymbol{\sigma}_K \cdot \mathbf{B}_0. \tag{2.2}$$

The shielding tensor is not directly observed in experiments, instead it appears through the chemical shift, δ_K, defined as

$$\delta_K = -(\sigma_K - \sigma_{K,\text{ref}}). \tag{2.3}$$

Here, σ_K is the nuclear magnetic shielding constant, which is normally of concern in high-resolution liquid- or gas-phase NMR, where molecules are free to rotate. As a result of the rotational averaging, the shielding constant equals the trace of the corresponding shielding tensor:

$$\sigma_K = \frac{1}{3}\sum_{\epsilon=x,y,z} \sigma_{K,\epsilon\epsilon}. \tag{2.4}$$

Furthermore, $\sigma_{K,\text{ref}}$ is the corresponding shielding constant in a well-characterised reference material. The Zeeman and hyperfine interactions between nuclei and electrons, which give rise to shielding constants, are exceedingly small and, thus, σ_K and δ_K are measured in ppm. In the solid state, the directional dependence of these interactions becomes observable and, $e.g.$, gives rise to the so-called chemical shift anisotropy (CSA) [16, 17, 30]. The shielding anisotropy with respect to the z-direction (selected normal to the material plane in the studied systems), is defined as

$$\Delta\sigma_K = \sigma_{K,zz} - \frac{1}{2}(\sigma_{K,xx} + \sigma_{K,yy}), \tag{2.5}$$

where x- and y-directions are in the molecular plane.

The rest of the terms in H_{NMR} contribute to the fine structure of the NMR spectrum. In the second term, the nuclear magnetic dipole moments of two different nuclei (K and L) are coupled with two different types of interaction mechanisms [16, 17, 27]. These are (1) the through-space classical dipole-dipole interaction expressed as $\mathbf{D}_{KL}$ and (2) the indirect mechanism occurring via the electrons, expressed as $\mathbf{J}_{KL}$ [31]. The last term in H_{NMR}, which appears in the presence of nuclei with $I_K \geq 1$, includes the quadrupole coupling $\boldsymbol{\mathcal{B}}_K$. Its magnitude can be written as [27]

$$\mathcal{B}_K = \frac{C_K}{2I_K(2I_K - 1)}, \tag{2.6}$$

where C_K is the nuclear quadrupole coupling constant. This is an observable resulting from the interaction of the non-spherical nuclear charge distribution and the electric field gradient (EFG) at the nuclear site. It can be expanded as the product of the so-called electric quadrupole moment eQ_K of nucleus K and the largest principal value[†] of the EFG

[†]A symmetric 2-index tensor can be represented in the coordinate frame called the principal axis system (PAS) where the tensor is fully diagonal. Principal values refer to the diagonal components in this frame, $V^{\text{PAS}} = \begin{pmatrix} V_{11} & 0 & 0 \\ 0 & V_{22} & 0 \\ 0 & 0 & V_{33} \end{pmatrix}$ [28].

tensor, V_{33}, as

$$C_K = \frac{eQ_K V_{33}}{h}. \tag{2.7}$$

In a high-resolution spectrum, the indirect spin-spin couplings average to the isotropic coupling constants, J_{KL}, and are measured in Hz. In contrast, the direct and quadrupole couplings average to zero in isotropic liquid and gas samples.

$\mathbf{D}_{KL}$ can be calculated from the positions of nuclei K and L using classical electromagnetism. All the other NMR parameters are intrinsically linked with the electronic ground state, modified by the different, weak perturbations [28, 32]. Therefore, in order to calculate NMR parameters, the electronic degrees of freedom are necessarily included explicitly. One needs to determine the dependence of the electronic energy on the magnetic field $\mathbf{B}_0$ and on the nuclear magnetic moments $\boldsymbol{\mu}_K$. For this purpose, an approximate electronic wavefunction of the system must be provided by reasonably accurate first-principles quantum-mechanical calculations.

The magnetic and Zeeman interactions are small compared to the interactions involved in chemical bonding. Hence, perturbation theory is justifiedly applied in calculating the NMR parameters from the electronic wavefunction [31]. The electronic energy expression can be expanded in the static perturbations introduced by the external magnetic field and nuclear magnetic moments in the form

$$\begin{aligned} E(\mathbf{B}_0, \{\mathbf{I}_K\}) =& E_0 + \mathbf{E}_{\mathrm{B}_0} \cdot \mathbf{B}_0 + \sum_K \mathbf{E}_{\mathrm{I}_K} \cdot \mathbf{I}_K + \frac{1}{2}\mathbf{B}_0 \cdot \mathbf{E}_{\mathrm{B}_0,\mathrm{B}_0} \cdot \mathbf{B}_0 \\ &+ \sum_K \mathbf{I}_K \cdot \mathbf{E}_{\mathrm{I}_K,\mathrm{B}_0} \cdot \mathbf{B}_0 + \frac{1}{2}\sum_{K,L} \mathbf{I}_K \cdot \mathbf{E}_{\mathrm{I}_K,\mathrm{I}_L} \cdot \mathbf{I}_L, \end{aligned} \tag{2.8}$$

when retaining up to second-order terms. Higher-order terms give small perturbations and can be neglected to the accuracy of ordinary NMR. Therefore, the comparison of the expansion (2.8) with H_{NMR} (2.1) leads to the definition of the NMR spectral parameters as the following derivatives of the perturbed energy:

$$\boldsymbol{\sigma}_K = \frac{1}{\gamma_K \hbar} \frac{\partial^2 E(\mathbf{I}_K, \mathbf{B}_0)}{\partial \mathbf{I}_K \partial \mathbf{B}_0}\bigg|_{\boldsymbol{\mu}_K = \mathbf{0}, \mathbf{B}_0 = \mathbf{0}} + \mathbf{1} \tag{2.9}$$

$$\mathbf{J}_{KL} = \frac{1}{h} \frac{\partial^2 E(\mathbf{I}_K, \mathbf{I}_L)}{\partial \mathbf{I}_K \partial \mathbf{I}_L}\bigg|_{\mathbf{I}_K = \mathbf{0}, \mathbf{I}_L = \mathbf{0}} - \mathbf{D}_{KL} \tag{2.10}$$

$$\boldsymbol{\mathcal{B}}_K = \frac{1}{h} \frac{\partial E(\mathbf{I}_K)}{\partial \mathbf{I}_K \mathbf{I}_K}\bigg|_{\mathbf{I}_K = \mathbf{0}}. \tag{2.11}$$

In the expansion (2.8), the first-order terms vanish for closed-shell systems. Furthermore, the term $\mathbf{E}_{\mathrm{B}_0,\mathrm{B}_0}$ corresponds to the magnetisability tensor that does not enter H_{NMR}. In the expression (2.9), $\mathbf{1}$ is the 3x3 unit matrix representing the bare-nucleus Zeeman interaction, present also in the absence of electrons.

In the practical computations of these and other molecular properties in this thesis, the material systems are treated as quantum-mechanical objects but the perturbations as classical electromagnetic fields. In particular, the magnetic resonance parameters introduced here and in the following sections, are calculated via time-independent and -dependent perturbations to the ground-state wavefunction.

2.2 Electron spin resonance

ESR is an analytical spectroscopic technique for systems with unpaired electrons [15, 31]. It gives local information of the atomic and electronic structure of, $e.g.$, material defects [18, 19]. The most important ESR spectral parameter is the g-tensor, which parametrises the Zeeman interaction of the magnetic moment of the unpaired electrons(s) with the externally applied magnetic field. Such a magnetic moment is defined as $\mathbf{m}_{\mathrm{e}} = \mu_{\mathrm{B}}\mathbf{g}\cdot\mathbf{S}$, where $\mu_{\mathrm{B}} = e\hbar/2m_e$ is the Bohr magneton and $\mathbf{S}$ the so-called effective spin. $\mathbf{S}$ combines the magnetic moments of the electron, having their origin in the spin (with the spin quantum number $s = 1/2$), and orbital motion. The Zeeman interactions in ESR are sensitive to the local geometric and electronic structure, because (similarly to the nuclear shielding in NMR) the g-shift tensor in ESR can be associated with the changes in the local magnetic field, induced by electronic currents [31]. The g-shift is defined as the difference $\Delta\mathbf{g} = \mathbf{g} - g_{\mathrm{e}}\mathbf{1}$ from the isotropic free-electron g-factor, $g_{\mathrm{e}} = 2.002319304$ [33]. Somewhat analogous to the spin-spin coupling in NMR, the coupling of the magnetic moment of the unpaired electrons with those of nuclei gives rise to the hyperfine coupling (HFC) tensor, $\mathbf{A}_K$. At the nonrelativistic limit, $\mathbf{A}_K$ consists of the isotropic contact and anisotropic dipolar coupling and contributes to the fine structure of the ESR spectrum.

The experimental ESR spectrum of the spin-1/2[‡] material defect can be interpreted in terms of the Hamiltonian (in energy units)

$$H_{\mathrm{ESR}} = \mu_{\mathrm{B}}\mathbf{B}_0\cdot\mathbf{g}\cdot\mathbf{S} + \sum_K \mathbf{S}\cdot\mathbf{A}_K\cdot\mathbf{I}_K, \tag{2.12}$$

where the Zeeman interaction term is bilinear in the effective electron spin and the applied magnetic field $\mathbf{B_0}$, and the hyperfine interaction term with $\mathbf{S}$ and the nuclear spins $\mathbf{I}_K$.

A consideration of the ESR spin Hamiltonian and the second term in the energy expression (2.8), in the presence of an "internal" perturbation $\mathbf{S}$, formally defines the g-tensor as a derivative of the perturbed energy

$$\mathbf{g} = \frac{1}{\mu_{\mathrm{B}}}\frac{\partial^2 E(\mathbf{B},\mathbf{S})}{\partial\mathbf{B}\partial\mathbf{S}}\bigg|_{\mathbf{B}=\mathbf{0},\mathbf{S}=\mathbf{0}}. \tag{2.13}$$

Correspondingly, consideration of H_{ESR} with the third term in the expression (2.8) leads to the definition of the hyperfine coupling tensor as

$$\mathbf{A}_K = \frac{\partial^2 E(\mathbf{I}_K,\mathbf{S})}{\partial\mathbf{I}_K\partial\mathbf{S}}\bigg|_{\mathbf{I}_K=\mathbf{0},\mathbf{S}=\mathbf{0}}. \tag{2.14}$$

2.3 Paramagnetic nuclear magnetic resonance

As compared to the standard NMR of closed-shell substances, in pNMR the chemical shifts are greatly enhanced, providing a kind of "magnifying glass" for paramagnetic systems.

[‡]In spin-1/2 paramagnetic centers, $\mathbf{m}_{\mathrm{e}}$ arises from one unpaired electron. For systems involving more than one unpaired electron, a third interaction term enters H_{ESR}, the so-called zero-field splitting [18].

This enhancement arises from the interaction of the nuclear spins with the comparatively large magnetic moment of the unpaired electron(s) [21]. In pNMR, an ensemble of $2S$+1 thermally populated states need to be considered. Besides the orbital contributions to the shielding tensor of nucleus K, $\boldsymbol{\sigma}_K^{\text{orb}}$, analogous to the shielding tensor of diamagnetic systems [34], one has to consider the explicitly temperature-dependent hyperfine shielding, which arises from the spin-dependent Fermi contact (FC) and spin-dipole (SD) hyperfine interactions [18]. The total shielding tensor in the case of a spin-half paramagnetic system can be written as [35]

$$\boldsymbol{\sigma}_K = \boldsymbol{\sigma}_K^{\text{orb}} - \frac{1}{\gamma_K \hbar} \frac{\mu_{\text{B}}}{kT} \frac{S(S+1)}{3} \mathbf{g} \cdot \mathbf{A}_K, \tag{2.15}$$

where the ESR parameters $\mathbf{g}$ and $\mathbf{A}_K$ appear. These two tensors may be analysed in terms of relativistic corrections, primarily for the present light-atom systems arising from the spin-orbit (SO) interaction. The correction terms arise in up to fourth order, $\mathcal{O}(\alpha^4)$ of the fine structure constant α [35, 36]. The SO-induced deviation of the g-tensor from the isotropic g_e-factor, appears explicitly in

$$\mathbf{g} = (g_{\text{e}} + \Delta g_{\text{iso}})\mathbf{1} + \Delta\tilde{\mathbf{g}}, \tag{2.16}$$

where Δg_{iso} is the isotropic and $\Delta\tilde{\mathbf{g}}$ the anisotropic part of the g-shift term. By this, first-principles calculation of the so-called pseudocontact and anisotropic contact contributions to the pNMR shielding tensor, were formalised in the spin-1/2 case [35]. A further extension was made in Ref. [36] by also including the SO-contributions to the HFC tensor, which resulted in the following expansion

$$\begin{aligned} \mathbf{A} &= A_{\text{con}}\mathbf{1} + \mathbf{A}_{\text{dip}} + \mathbf{A}_{\text{SO}} \\ &= (A_{\text{con}} + A_{\text{PC}})\mathbf{1} + \mathbf{A}_{\text{dip}} + \mathbf{A}_{\text{dip,2}} + \mathbf{A}_{\text{as}}. \end{aligned} \tag{2.17}$$

Here, the relativistic, $\mathcal{O}(\alpha^4)$ terms contain the isotropic spin-orbit correction A_{PC}, the anisotropic but symmetric (rank-2) spin-dipole term $\mathbf{A}_{\text{dip,2}}$, and the anisotropic and anti-symmetric term, $\mathbf{A}_{\text{as}}$.

The hyperfine shielding terms arising from the product $\mathbf{g} \cdot \mathbf{A}_K$ in equation (2.15), read as follows:

$$\begin{aligned} \mathbf{g} \cdot \mathbf{A}_K =& g_e A_{\text{con}}\mathbf{1} + g_e \mathbf{A}_{\text{dip}} \\ &+ g_e A_{\text{PC}}\mathbf{1} + g_e \mathbf{A}_{\text{dip,2}} + g_e \mathbf{A}_{\text{as}} \\ &+ \Delta g_{\text{iso}} A_{\text{con}}\mathbf{1} + \Delta g_{\text{iso}} \mathbf{A}_{\text{dip}} \\ &+ \Delta\tilde{\mathbf{g}} A_{\text{con}} + \Delta\tilde{\mathbf{g}} \cdot \mathbf{A}_{\text{dip}}. \end{aligned} \tag{2.18}$$

In the former expansion, a total of four terms contain a tensorial rank-0 part (the terms involving $\mathbf{1}$ and the $\Delta\tilde{\mathbf{g}} \cdot \mathbf{A}_{\text{dip}}$ term) in the $S = 1/2$ case, and thus contribute to the isotropic chemical shift. Three of them, $g_{\text{e}} A_{\text{con}}$, $g_{\text{e}} A_{\text{PC}}$, and $\Delta g_{\text{iso}} A_{\text{con}}$, have similar transformation properties and constitute together the contact shift [37]. When the paramagnetic system consists only of light atoms, a major contribution to the chemical shift comes from the first term. $\Delta\tilde{\mathbf{g}} \cdot \mathbf{A}_{\text{dip}}$ is the term that determines the experimentally important pseudocontact shift. It arises from the long-range dipolar interaction of the nuclear and electronic spins, mediated by the anisotropic part of the g-tensor. The latter can be empirically related

Table 2.1. The hyperfine shielding terms resulting from the product $\mathbf{g} \cdot \mathbf{A}_K$ in equation (2.15), arranged in the appropriate order in the fine structure constant α and the tensorial rank, in a spin-1/2 paramagnetic system.

Product $\mathbf{g} \cdot \mathbf{A}_K^a$	Nature of the term	Order in α	Tensorial rank[b]
$g_\mathrm{e} A_\mathrm{con}$	Nonrelativistic contact	α^2	0
$g_\mathrm{e} \mathbf{A}_\mathrm{dip}$	Nonrelativistic dipolar	α^2	2
$g_e A_\mathrm{PC}$	Contact from SO to $\mathbf{A}$	α^2	0
$g_e \mathbf{A}_\mathrm{dip,2}$	Dipolar from SO to $\mathbf{A}$	α^4	2
$g_e \mathbf{A}_\mathrm{as}$	Antisymmetric from SO to $\mathbf{A}$	α^4	1
$\Delta g_\mathrm{iso} A_\mathrm{con}$	Contact from SO to $\mathbf{g}$	α^4	0
$\Delta g_\mathrm{iso} \mathbf{A}_\mathrm{dip}$	Dipolar from SO to $\mathbf{g}$	α^4	2
$\Delta \tilde{\mathbf{g}} A_\mathrm{con}$	Anisotropic contact	α^4	2
$\Delta \tilde{\mathbf{g}} \cdot \mathbf{A}_\mathrm{dip}$	Pseudocontact	α^4	0,2

[a] g_e is the free electron g-factor, A_con and $\mathbf{A}_\mathrm{dip}$ the isotropic and dipolar hyperfine couplings, and Δg_iso and $\Delta \tilde{\mathbf{g}}$ are the isotropic and anisotropic parts of the g-shift tensor. The spin-orbit correction to $\mathbf{A}$ (lines 3-5), contains the isotropic A_PC term as well as the symmetric $\mathbf{A}_\mathrm{dip,2}$ and antisymmetric $\mathbf{A}_\mathrm{as}$ anisotropic terms. In Paper III, these three terms are omitted due to their very small contributions for the studied systems containing only light H, C, and F atoms [36, 38]. [b] The rank-0 contribution corresponds to the isotropic shielding constant, as well as the rank-1 and 2 contributions to the antisymmetric and symmetric parts of the anisotropic shielding, respectively.

to the magnetisability (susceptibility) of the system [20]. In the study presented in this thesis, the HFC tensor is calculated at the NR limit and hence the terms including A_PC, $\mathbf{A}_\mathrm{dip,2}$, and $\mathbf{A}_\mathrm{as}$, which arise from the SO-corrections to $\mathbf{A}$, are omitted. This is not a severe approximation in the present case of light-element systems [36, 38]. Hence, the isotropic hyperfine shielding terms considered presently are $g_\mathrm{e} A_\mathrm{con}$, $\Delta g_\mathrm{iso} A_\mathrm{con}$, and $\Delta \tilde{\mathbf{g}} \cdot \mathbf{A}_\mathrm{dip}$. Correspondingly, five terms in equation (2.18) have tensorial rank-2 parts. After excluding one of them, $\mathbf{A}_\mathrm{dip,2}$, the anisotropic terms contained in the present calculations are $g_\mathrm{e} \mathbf{A}_\mathrm{dip}$, $\Delta g_\mathrm{iso} \mathbf{A}_\mathrm{dip}$, $\Delta \tilde{\mathbf{g}} A_\mathrm{con}$, and $\Delta \tilde{\mathbf{g}} \cdot \mathbf{A}_\mathrm{dip}$. Table 2.1 summarises the hyperfine shielding terms.

2.4 Faraday magneto-optic rotation

In optically active media, the polarisation plane of linearly polarised light (LPL) rotates when it impinges into the transparent regions of the sample [22, 23, 31]. The rotation results due to the difference of the refractive indices n_- for left- and n_+ for right-circular components of LPL, $\Delta n = n_- - n_+$. An isotropic medium of chiral molecules as well as a solid possessing enantiomorphism in its crystal structure ($e.g.$, quartz) [39], exhibit this circular birefringence without an external magnetic field, in a phenomenon known as natural optical activity [31]. In the presence of an external magnetic field the rotation occurs for any type of matter [40]. Depending on the geometrical setup and polarisation status, which can be linear, circular or elliptic, many different types of field-induced

magneto-optic effects have been observed [22]. In the Faraday rotation experiment, a static magnetic field is applied parallel with the direction of the LPL beam [23].

The Faraday optical rotation (FOR) arises thus from circular birefringence due to the differential interaction of the medium with the left- and right-circularly polarised components of the LPL. The interaction involves two oscillating, mutually perpendicular dipole moments. The rotation angle θ can be obtained as

$$\theta = \frac{\pi l}{\lambda}\Delta n, \tag{2.19}$$

where λ is the wavelength of light and l is the optical path length in the medium. Generally, the index of refraction is a two-index tensor that is related to the polarisability tensor $\alpha_{\epsilon\tau}$ as [41]

$$n_{\epsilon\tau} = \delta_{\epsilon\tau} + \frac{\mathcal{N}}{2\epsilon_0}\langle\alpha_{\epsilon\tau}\rangle, \tag{2.20}$$

when $n \approx 1$ (in low-density medium). Here, $\mathcal{N}$ is the number density of molecules and $\langle\alpha_{\epsilon\tau}\rangle$ is the averaged polarisability due to molecular tumbling in the medium.

In the presence of a magnetic interaction, the wavefunction that describes the electron cloud becomes complex and furthermore the complex polarisability contains both symmetric rank-2 and antisymmetric rank-1 parts. It is the antisymmetric part, $\alpha'_{\epsilon\tau}$, that gives rise to the rotation and, due to the smallness of magnetic perturbations, can be expanded as a power series in terms of the external magnetic field $\mathbf{B}_0$ and the nuclear spin $\mathbf{I}_K$, retaining only the first order terms [25, 40–42]

$$\alpha'_{\epsilon\tau}(\omega) = \sum_{\nu}\alpha'^{(B_0)}_{\epsilon\tau,\nu}B_{0,\nu} + \sum_{\nu}\alpha'^{(I_K)}_{\epsilon\tau,\nu}I_{K,\nu} + \mathcal{O}(B_0^3, I_K^3). \tag{2.21}$$

Here, ω is the angular frequency of the light and $\epsilon\tau\nu$ are the Cartesian xyz coordinates in the molecule-fixed frame. In this expression, the terms involving the $\alpha'^{(B_0)}$ and $\alpha'^{(I_K)}$ coefficients give rise to FOR and NSOR, respectively. The isotropic rotational average of the antisymmetric polarisability in the laboratory frame, in the case of FOR with the magnetic field in the Z direction of the light beam, is obtained from the expression

$$\langle\alpha'_{XY}\rangle = \frac{1}{6}B_0\sum_{\epsilon\tau\nu}\epsilon_{\epsilon\tau\nu}\alpha'^{(B_0)}_{\epsilon\tau,\nu} = \frac{B_0}{3}\left[\alpha'^{(B_0)}_{xy,z} + \alpha'^{(B_0)}_{yz,x} + \alpha'^{(B_0)}_{zx,y}\right], \tag{2.22}$$

where $\epsilon_{\epsilon\tau\nu}$ is the Levi-Civita symbol. The corresponding expression for NSOR can be obtained by replacing $\alpha'^{(B_0)}_{\epsilon\tau,\nu}$ by $\alpha'^{(I_K)}_{\epsilon\tau,\nu}$ and the amplitude of the field, B_0, by the average spin polarisation $\langle I_{K,Z}\rangle$ in the direction of the propagation of the beam.

In the case of FOR, the rotation angle is parameterised as

$$\Phi_{\text{FOR}} = V(\omega)B_0 l, \tag{2.23}$$

where V is the Verdet constant [22], which is obtained from the frequency-dependent α'_{XY}. On the other hand, in NSOR, α'_{XY} is activated by the magnetisation of nuclei and, therefore, the rotation angle is parameterised by the nucleus-specific NSOR constant, $V_K(\omega)$ [43, 44], instead of the system-specific Verdet constant of FOR. In general, this type of nuclear spin-induced magneto-optic effects offer a new and growing family of proposed spectroscopies to investigate materials with a resolution that is, in principle, limited by the diffraction limit of the probe light.

3 Methods

3.1 Electronic structure calculations

In order to predict the spectral parameters or any electronic properties, a good approximation for the electronic wavefunction has to be known. This many-body problem is an impossible task to solve exactly even for the simplest molecular system. Thus, in every practical quantum-chemical investigation, accurate approximations are used [31, 45]. The very first simplification is the decoupling of the dynamics of the electrons and nuclei. This is known as the Born-Oppenheimer approximation [46], where the large difference of the nuclear and electron masses justifies treating only the dynamics of electrons quantum-mechanically, with the nuclei constituting a fixed framework. This allows expressing the collective behaviour of the electrons via the time-independent Schrödinger equation

$$H\psi = E\psi, \tag{3.1}$$

where E is the energy of the system and ψ is the wavefunction. H is the Hamiltonian, an operator in which the electronic kinetic energy as well as the electron-nucleus and electron-electron interactions are included. Another essential source of relief from the complexity of the task, in the case of light-atom systems, is the possibility of nonrelativistic (NR) treatment of electrons. Then,

$$H = -\frac{\hbar^2}{2m_e}\sum_{i}^{N_e}\nabla_i^2 - \frac{e^2}{4\pi\epsilon_0}\sum_{i}^{N_e}\sum_{K}^{N_n}\frac{Z_K}{r_{iK}} + \frac{1}{2}\frac{e^2}{4\pi\epsilon_0}\sum_{i\neq j}^{N_e}\frac{1}{r_{ij}}, \tag{3.2}$$

where the summations run over the all N_e electrons and N_n nuclei. The motions of electrons are still correlated with each other, preserving the problems of many-body interactions. The nature of the electron-electron interaction includes both Coulombic repulsion of the charges and the purely quantum-mechanical exchange interaction, arising from the fermionic character of the electrons [31]. The latter aspect implies that the Pauli exclusion principle has to be obeyed, setting the antisymmetry requirement for the many-electron wavefunction under the exchange of any two electrons of the system. This requirement enforces a spatial separation between electrons of the same spin, which reduces the energy of the system by the so-called exchange energy. Electron correlation

leads in principal to the treatment of 3^{N_e} coordinates for an N_e-electron system, and an insurmountable complexity of the problem. Practical solutions to the many-body problems such as this, are based on methods in which the Coulomb interactions are treated approximately [31, 45].

Hierarchic improvements in a series of approximations can be based on the variational principle, which states the upper limit of the true ground-state energy as resulting from an approximate wavefunction [31, 45, 47]. In quantum chemistry, the fundamental first step in such a series of *ab initio* theories rests on the Hartree-Fock (HF) approach [48, 49], where the exchange interaction is accurately included, because the wavefunction consists of an antisymmetrised product of independent-electron wavefunctions, orbitals. The HF wavefunction is a Slater determinant which includes all possible permutations of pairs of electrons [31, 47]. Hence, the HF method contains the exchange but does not include the instantaneous Coulomb interactions, only their average. Sophisticated approximations to treat those interactions more completely, are constituded by post-HF methods [47, 50], which reduce the Coulomb energy as compared to HF. This energy difference is called the correlation energy.

In the HF method, the computational cost of the calculations increases as the fourth power of the number of basis functions*, $\mathcal{O}(N^4)$ [50]. An inclusion of the correlation energy even in a relatively coarse manner scales up the cost tremendously. Therefore, an alternative way to treat correlation has been developed. Density-functional theory (DFT) [51] is the most popular electronic structure method especially for large molecules and solids. Similarly to HF, DFT is an effective one-electron theory and the two methods share also many other similarities. The reason for the popularity of DFT relies in its inclusion of electron correlation in effectively the same computational cost as that of a corresponding HF calculation. The downside of DFT is in the approximate treatment of both exchange and correlation energies, which renders the systematic improvement of the calculations difficult†. For that reason, calculations by the contemporary DFT methods should be calibrated against the results of more accurate post-HF methods, or experimental results.

3.1.1 Density-functional theory

In DFT, the total energy, including exchange and correlation contributions, is calculated from the knowledge of the electronic charge density ρ at all locations in the system [51]. Therefore, the 3^{N_e} degrees of freedom of the many-body wavefunction are reduced to only three dimensions (x, y, z) of the density and the spin coordinate, regardless how many electrons the system has [31].

In the Kohn-Sham (KS) formulation [55] of DFT, the ground-state density $\rho(\mathbf{r})$ is defined in terms of the hypothetical noninteracting KS reference state, described by a

*A linear combination of basis functions constitute the representations for single-electron states and, therefore, are involved in the solution of the electronic structure, *vide infra*.

†In HF the exchange potential is nonlocal while in DFT it must be local. There are attempts at systematic improvement of DFT by the construction of exact and, at the same time, local exchange, $e.g.$, in the optimised effective potential (OEP) [52] and localised Hartree-Fock (LHF) [53] methods. So far these methods have not been implemented in widely available codes capable of molecular property calculations. The issue is still in progress [54].

single Slater determinant consisting of one-electron KS orbitals ψ_i. The reference system has the same density as the real interacting system,

$$\rho(\mathbf{r}) = \sum_{i=1}^{N_e} |\psi_i|^2 . \tag{3.3}$$

By varying the KS orbitals, the minimum value of the total energy functional corresponds to the approximate ground-state energy of the system.

In the KS formalism, the interacting many-electron system is, hence, mapped onto a system of fictitious noninteracting electrons that move in an effective KS potential, v_{eff}, arising due to the nuclei and electrons. This mapping leads to a set of N_e single-particle Schrödinger-like equations, called KS equations [51, 56],

$$-\frac{\hbar^2}{2m_e}\nabla^2\psi_i(\mathbf{r}) + v_{\text{eff}}(\mathbf{r})\psi_i(\mathbf{r}) = \epsilon_i\psi_i(\mathbf{r}), \tag{3.4}$$

where ϵ_i are the orbital energies. The KS potential is defined as

$$v_{\text{eff}}(\mathbf{r}) = V_{\text{ion}}(\mathbf{r}) + V_{\text{H}}(\mathbf{r}) + V_{\text{xc}}(\mathbf{r}), \tag{3.5}$$

where V_{ion} is the nuclei-electron Coulomb potential and V_{H} is the Hartree potential from the average density of the electrons, defined as

$$V_{\text{H}}(\mathbf{r}) = \frac{e^2}{4\pi\epsilon_0}\int \frac{\rho(\mathbf{r}')}{|\mathbf{r}+\mathbf{r}'|}d\mathbf{r}'. \tag{3.6}$$

The exchange-correlation potential V_{xc} is given as the functional derivative of the exchange-correlation energy, which contains also a contribution due to the difference of the kinetic energy between the true and noninteracting systems

$$V_{\text{xc}}(\mathbf{r}) = \frac{\delta E_{\text{xc}}[\rho(\mathbf{r})]}{\delta\rho(\mathbf{r})}. \tag{3.7}$$

The fact that the KS potential depends on the electron charge density, which is built from KS orbitals, sets the requirement that the KS equations need to be solved in a self-consistent manner. The procedure starts from an initial guess of ρ that, $e.g.$, can be constructed by superimposing atomic densities [45] or using the Hückel approximation [31]. This density is used for the computation of V_{H} and V_{xc}, which are furthermore used for the construction of $v_{\text{eff}}(\mathbf{r})$. After the first iteration, KS-orbitals allow defining an improved density from the expression (3.3). The process is repeated until self-consistency of the solutions is obtained, within the chosen numerical precision [31, 56]. The total energy can be determined from the converged density, which is a function of position, through [51]

$$E = \sum_{i=1}^{N_e}\epsilon_i - \frac{1}{2}\frac{1}{4\pi\epsilon_0}\iint\frac{\rho(\mathbf{r})\rho(\mathbf{r}')}{|\mathbf{r}+\mathbf{r}'|}d\mathbf{r}d\mathbf{r}' + E_{\text{xc}}[\rho(\mathbf{r})] - \int V_{\text{xc}}\left[\rho(\mathbf{r})\right]\rho(\mathbf{r})d\mathbf{r}. \tag{3.8}$$

What still remains a fundamental problem in DFT, is the fact that the exact form of the functional $E_{\text{xc}}[\rho(\mathbf{r})]$ is unknown and needs to be estimated approximately. The local

density approximation (LDA) [55] provides the simplest useful model for $E_{\mathrm{xc}}[\rho(\mathbf{r})]$ and is used successfully mainly in solid-state studies [56]. In LDA, the exchange-correlation energy at a given point $\mathbf{r}$ is taken to be the same as in a uniform electron gas with the same charge density. Due to this, LDA can be thought to work well for systems with slowly varying electron density. Therefore, for molecules and solids with rapidly varying electron density, as well as many spectroscopic properties, LDA provides only a poor description. Generalised gradient approximation (GGA) [31] constitutes a great improvement in the sense that the energy depends not only on the local uniform density, but also its gradient, $E_{\mathrm{xc}}^{\mathrm{GGA}} = E_{\mathrm{xc}}[\rho(\mathbf{r}), \nabla\rho(\mathbf{r})]$. Compared to LDA, GGA gives better results for molecular geometries and properties [57][‡].

Numerous different GGA functionals have been proposed, varying in the parameters of the exchange and correlation contributions [58]. The parameters that ultimately determine the difference between the functionals, can be obtained from theoretical or semi-empirical constraints. The GGA functional by Perdew, Burke, and Ernzerhof (PBE) [60] gives reasonably accurate bond lengths and is, hence, one of the most popular GGAs for geometry optimisation. Similarly to most GGAs, PBE underestimates the energy gap between the occupied and unoccupied states. Despite this fundamental difficulty, PBE has been used successfully for many molecular and solid-state properties, also for the computation of magnetic resonance. In the NMR chemical shift, the success of PBE is partially based on error cancellation with the chemical shift reference system, resulting in some cases from the electronic similarities of the reference and studied systems. Another source of error cancellation is operative in the inner atomic shells of the systems that remain similar regardless the chemical environment.

Hybrid functionals tune the exchange energy by including a fraction of the exact Hartree-Fock exchange, calculated from the Slater determinant of the KS orbitals [45]. In the case of NMR, the exact exchange improves results for nuclear shieldings due to the dependence of this property on the occupied-unoccupied energy differences [57]. The hybrid functional means extra computational work but is feasible in quantum-chemical calculations based on localised orbital basis sets. In contrast, in solid-state systems with periodic boundary conditions and extended basis, the hybrid functionals require a large computational effort and have not been applied for the NMR properties, yet [61]. Because the optimum amount of exact exchange is not universal, there are many families of hybrid functionals available, including some in which the correlation part remains the same but the proportion of the HF exchange is gradually increased. Particularly popular is the family that uses the correlation part by Lee, Yang, and Parr (LYP) [62] and exchange parts with 0% (in the BLYP functional) [62, 63], 20% (B3LYP) [62, 64, 65], and 50% (BHandHLYP) [62, 64] admixture of the exchange functional by Becke [63, 64] and the exact HF exchange.

All studies done in this thesis are based on the DFT framework. The PBE functional was used for all geometry optimisations. It provided the exchange and correlation for the NMR properties in Paper I as well as for the ESR and pNMR properties in Paper III. In contrast, the B3LYP hybrid functional was used in Papers II and IV, where the ^{13}C NMR spectral patterns as well as the Faraday rotation and NSOR constants were predicted, respectively.

[‡]Functionals based on higher derivatives, beyond GGAs, and also on the derivative of kinetic energy density, are collectively termed as meta-GGAs [58]. One of the most successful such attempts is the TPSS functional [59]. So far, meta-GGAs are not widely used for magnetic properties [57].

3.1.2 Molecular representation

In order to solve numerically the single-electron eigenvalue problems of the previous section, the KS orbitals have to be represented in terms of a basis set that has to, for the purpose of practical computations, be of finite size. In a molecular quantum chemistry calculation, the molecular orbitals ψ are constructed from a set of atom-centered basis functions χ_μ as [31, 45, 47, 66, 67]

$$\psi = \sum_\mu c_{\mu i} \chi_\mu, \tag{3.9}$$

which is the so-called linear combination of atomic orbitals (LCAO). Here, the c_i are the expansion coefficients that become variationally optimised during the self-consistent field (SCF) calculation. In the SCF procedure, the KS equations are written as the matrix equation [66, 67]

$$\mathbf{F}^{\mathrm{KS}}\mathbf{C} = \mathbf{S}\mathbf{C}\boldsymbol{\epsilon}, \tag{3.10}$$

where $\mathbf{S}$ is the overlap matrix defined as $S_{\mu\nu} = \langle \chi_\mu | \chi_\nu \rangle$. $\mathbf{F}^{\mathrm{KS}}$ is the KS matrix containing individual interaction terms of Eq. (3.4). It depends on the solutions included in the orbital coefficient matrix $\mathbf{C}$. $\boldsymbol{\epsilon}$ is the diagonal orbital energy matrix.

Gaussian functions constitute the most common choice for the atomic orbitals, defined as [68]

$$\chi_\mu(r, \theta, \phi) = Y_{lm}(\theta, \phi)\, r^l e^{-\zeta r^2}, \tag{3.11}$$

where r is the distance from the particular nucleus, $Y_{lm}(\theta, \phi)$ are the spherical harmonics for certain angular momentum (l) and magnetic (m) quantum numbers, and ζ is the so-called exponent of the basis function. The success and popularity of Gaussian-type orbitals (GTOs), despite the fact that the Gaussian functions cannot exactly reproduce the nuclear cusp or the asymptotic behaviour of the wavefunction at large distances [47, 69], stems from the Gaussian product theorem [31]. The theorem speeds up the calculation of the two-electron integrals that are needed to describe the Coulomb and exchange interactions of electrons. According to the theorem, a product of two Gaussians can be replaced by a single Gaussian centred at an intermediate position. In practical calculation, the inner orbitals, being largely independent of the chemical environment, are described by contracted GTOs. They are linear combinations of several individual, so-called primitive GTOs (3.11), having coefficients based on atomic calculations. Thus the use of contracted GTOs reduces the number of $c_{\mu i}$ coefficients and computational work. To overcome the physical insufficiency of GTOs, many GTOs or contracted GTOs are used [69]. Also numerical and Slater-type of functions are used in molecular electronic structure theory [45]. The latter deviate from the Gaussian form in their exponential factor, $e^{-\zeta r}$. Actually, Slater-type orbitals were the first to be used due to the benefit of their correct short- and long-distance atomic description [31, 45, 47]. Contrary to GTOs, STOs are incapable of representing two-electron integrals efficiently, limiting the utility of STOs in molecular systems [50].

Traditionally basis sets are optimised using atomic energy as the criterion. Molecular hyperfine properties present rather high demands to the quality of the basis. The involved

perturbation operators in the case of NMR contain high inverse powers of the distance between electrons and nuclei, presenting severe requirements for the proper description of electron density not only in the valence region but also close to nuclei. Hence, for computations of NMR parameters, the basis set has to contain so-called diffuse basis functions with small exponents ζ for the valence, as well as tight functions with large exponents for the inner region [69]. Therefore, performing calculations on large systems including hundreds of atoms, with these kinds of demands on the basis-set flexibility, becomes extremely heavy, sometimes impossible on the available computational resources. The completeness optimisation (co) method [70] offers a way to generate Gaussian basis sets that are both compact and enable nearly basis-set converged calculations for large molecules. The co paradigm is based on the idea that the sufficient ranges of exponents are first found and subsequently represented by a small number of functions, which are optimised systematically toward the basis-set limit.

In molecular calculations carried out in this thesis, only GTO basis sets have been used. All geometry optimisations have been performed with the def2-TZVP [71] basis, which is commonly used for that purpose giving good geometries at the DFT level. Both the NMR and Faraday rotation calculations, in Papers I, II and IV, were performed for relatively large graphenic systems. In these calculations we used the co basis sets, which were generated for such purposes, and which enabled predictions of the spectral parameters within close proximity to the basis-set limit.

3.1.3 Solid-state representation

Any solid material consists of a macroscopic number of electrons and nuclei. For a DFT calculation this means a practically infinite number of non-interacting electrons moving in the effective KS potential. This implies also an infinite number of orbitals extending all over the solid. This problem is solved by using the periodic boundary conditions and the Bloch theorem, which make use of the periodic potential underlying the concept of electronic band structure [56, 72]. The Bloch theorem allows representing the electronic states as so-called Bloch states and considering only one unit cell in the reciprocal space, $i.e.$, the first Brillouin zone. Due to the periodic boundary conditions, the effective one-electron KS Hamiltonian is translationally invariant, $v_{\text{eff}}(\mathbf{r}) = v_{\text{eff}}(\mathbf{r} + \mathbf{R})$, for all lattice vectors $\mathbf{R}$ of the crystal and, furthermore, the one-electron wavefunctions can be expressed as a linear combination of plane waves

$$\psi_{n,\mathbf{k}}(\mathbf{r}) = \sum_{\mathbf{G}} c_{n,\mathbf{k}+\mathbf{G}} e^{i(\mathbf{k}+\mathbf{G})\cdot\mathbf{r}}, \tag{3.12}$$

where the sum is over all reciprocal lattice vectors $\mathbf{G}$, defined by $\mathbf{G} \cdot \mathbf{R} = 2\pi m$. The $c_{n,\mathbf{k}+\mathbf{G}}$ are the coefficients of the KS one-electron states (*vide infra*). The electronic states are labelled by their crystal wave vector $\mathbf{k}$ and band index n.

According to the above expression, the Bloch theorem converts a calculation of an infinite number of electrons to the calculation of a finite number of bands at an, in principle, infinite number of k-points. The practical calculations are based on the approximation that the wavefunctions at adjacent k-points are almost identical and over a region of the

k-space can be represented by the wavefunction at a single k-point. Therefore, the occupied electronic states, which determine the electronic potential, total energy and other ground-state properties, are only required at a finite set of k-points. In systems with finite energy gap between the occupied and unoccupied states, $i.e.$, insulators and semiconductors, only a relatively small number of k-points may be needed to define the Fermi surface. In contrast, gapless systems, $i.e.$, metals and semimetals, require a much denser sets of k-points and, hence, demand more computational work. To reduce the number of the required k-points for such demanding systems, smearing methods have been developed [73, 74]. A great reduction of the computational load is provided by symmetry operations allowed by the system, $e.g.$, rotations and reflections, which reduce the problem to only the k-points of the symmetry-independent region of the Brillouin zone. In the studies of this thesis, the commonly used method consisting of an equidistant mesh of k-points, proposed by Monkhorst and Pack [75], is employed.

There are a number of different approaches to solve the KS equations. One important way by which they differ, is in the choice of the basis-set expansion. For periodic systems the most obvious choice is the plane-wave approach (3.12) [56, 61, 76], but also atomic orbitals are used with various function types [77, 78]. The advantage of the plane-wave basis is their simple form and the fact that they naturally extend through the entire space, compatibility with the periodic boundary conditions and, therefore, the representation being equivalent to a Fourier series [45]. Then, the KS equations can be expessed in the following form [56]

$$\sum_{\mathbf{G}'}\Bigg[\frac{\hbar^2}{2m_e}|\mathbf{k}+\mathbf{G}|^2\delta_{\mathbf{G}\mathbf{G}'}+V_{\text{ion}}(\mathbf{G}-\mathbf{G}')+V_{\text{H}}(\mathbf{G}-\mathbf{G}') + V_{\text{xc}}(\mathbf{G}-\mathbf{G}')\Bigg]c_{n,\mathbf{k}+\mathbf{G}'}=\epsilon_{n,\mathbf{k}}c_{n,\mathbf{k}+\mathbf{G}'}, \tag{3.13}$$

where the summation is over the reciprocal lattice vectors $\mathbf{G}'$. The first, kinetic energy term is diagonal in the plane-wave basis, hence the Kronecker symbol $\delta_{\mathbf{G}\mathbf{G}'}$, and the coefficients $c_{n,\mathbf{k}+\mathbf{G}'}$ are determined during the SCF procedure. The size of the Hamiltonian matrix, which sets the computational cost, is determined by the maximum value of the kinetic energy component. The choice of the cutoff energy E_{cut}, truncates the plane-wave expansion to a finite size, as

$$\frac{\hbar^2}{2m_e}\left|\mathbf{k}+\mathbf{G}\right|^2 \leq E_{\text{cut}}. \tag{3.14}$$

Similarly to the case of localised basis functions (such as GTOs), employing a finite basis set requires one to perform an appropriate basis-set convergence test to find desired computational accuracy for the property of interest. This is easily done in the plane-wave basis, where the completeness is controlled by a single parameter, E_{cut}. Additionally, the adequacy of the used k-sampling needs to be tested in a periodic calculation.

In order to maintain orthogonality with the core-states in the so-called all-electron calculations, the valence wavefunction is forced to undergo rapid oscillations, which necessitates using a very large plane-wave cut-off energy. This would lead to a prohibitive size of the KS Hamiltonian matrix, defined in equation (3.13). In practical solid-state

calculations, this issue is surmounted by the pseudopotential method [79], in which the core-valence interactions are covered by an effective potential. The core electrons are absorbed into the pseudopotential and only the valence electrons are explicitly considered. The use of pseudopotentials enables representing the valence wavefunctions by nodeless and smooth pseudo-wavefunctions, $\widetilde{\psi_n}$, which can be to constructed from a drastically smaller-size basis-set expansion than the corresponding all-electron wavefunctions. Outside of the core region, the parameters of the pseudopotentials are adjusted to reproduce the angular momentum-dependent all-electron wavefunctions. In the core region, the pseudo-valence electron density $\widetilde{n}^{\text{PS}}(\mathbf{r})$ has a non-physical form and is unsuitable for, $e.g.$, calculations of nucleus-specific spectral parameters.

The projector-augmented wave (PAW) method [80] introduced by Blöchl can be used to reconstruct from the pseudowavefunction the all-electron density $n_c^{\text{AE}}(\mathbf{r})$ in the region close to the nucleus. This provides the theoretical basis for core-electron specific calculations. In the PAW scheme, a linear transformation operator $\mathcal{T}$ that uses predefined projectors to certain atomic states, is used to map the valence pseudowavefunctions onto the corresponding, atom-centered all-electron wavefunctions.

3.2 Magnetic perturbations

The calculation of magnetic resonance parameters in the quantum-chemical scene is traditionally based on the interaction terms of the molecular electronic Breit-Pauli Hamiltonian, H_{BP} [28, 32]. H_{BP} is the two-component, limiting form of the relativistic Dirac-Coulomb-Breit Hamiltonian [81], in the presence of electromagnetic field. Staying within the Born-Oppenheimer approximation, the atomic nuclei are treated as stationary sources of fields. In the NR limit for the NMR and ESR spectral parameters, the necessary H_{BP} terms include the $\mathcal{O}(\alpha^0)$ orbital Zeeman interaction with the external magnetic field, $\mathcal{O}(\alpha^2)$ hyperfine interactions with nuclear spins and, for the ESR g-tensor, the $\mathcal{O}(\alpha^2)$ spin-orbit interaction. In the absence of relativistic corrections the resulting spectroscopic parameters are considered up to $\mathcal{O}(\alpha^2)$ (NMR shielding, ESR HFC), or $\mathcal{O}(\alpha^4)$ (NMR J-coupling, pNMR shielding).

The vector potential $\mathbf{A}^{\text{tot}}$ determines the magnetic field that is experienced at the location $\mathbf{r}$, as $\mathbf{B}^{\text{tot}}(\mathbf{r}) = \nabla \times \mathbf{A}^{\text{tot}}(\mathbf{r})$. For NMR shielding, the vector potential has two sources [28, 69]. First, a term associated with the external magnetic field, $\mathbf{A}_0(\mathbf{r})$, is defined as

$$\mathbf{A}_0(\mathbf{r}_i) = \frac{1}{2}\mathbf{B}_0 \times \mathbf{r}_{iO}, \tag{3.15}$$

where $\mathbf{r}_O = \mathbf{r} - \mathbf{O}$ specifies the location of the electron with respect to the gauge origin $\mathbf{O}$. The second source arises from the nuclear magnetic moment, expressed as

$$\mathbf{A}_K(\mathbf{r}) = \frac{\mu_0}{4\pi}\frac{\mathbf{m}_K \times \mathbf{r}_K}{r_K^3}, \tag{3.16}$$

where $\mathbf{r}_K = \mathbf{r} - \mathbf{R}_K$ defines the position from the nucleus K. In H_{BP}, magnetic operators that arise from $\mathbf{B}_0$, are influenced by the choice of the gauge origin of the vector potential. To be free of the spurious gauge-origin dependence, $i.e.$, in order for the calculated

properties to be translationally invariant, the calculations would require an infinitely large LCAO basis in molecular quantum chemistry [69] or, respectively, an infinite number of projectors in PAW-based solid-state calculations [61].

Specific techniques have been developed to surmount the gauge-origin problem. In the LCAO framework, the gauge-including atomic orbital (GIAO) [82, 83] method is a standard way to ensure the gauge independence of the results. The GIAO method attaches a field-dependent phase factor to the basis functions centered at atomic nuclei, by which it effectively transfers the local gauge origin to the natural location, the nucleus in question.

In solid-state calculation the form of the vector potential (3.15) is, in principle, incompatible, because the position operator does not have the periodicity of the lattice. A magnetic field can, however, be introduced by making it periodic but with a long wavelength, and by calculating the magnetic response of the electron system by density-functional perturbation theory (DFPT) [84]. In the limit of infinite wavelength, the $\mathbf{B}_0$-field is uniform, and one can use plane waves (Eq. 3.12) as the basis set. For solids, the calculation of gauge-dependent properties became possible when Pickard and Mauri [85] introduced a GIAO-like field-dependent transformation operator $\mathcal{T}_{\mathbf{B}}$ that, within the PAW scheme, imposes the translational invariance exactly. The method is known as the gauge-including projector augmented wave (GIPAW) approach.

3.2.1 Computation of response

The response function theory [86] provides a convenient way to reformulate time-dependent perturbation theory for quantum-chemical calculations in the molecular framework. The method allows to calculate the expectation value of an observable A when the system is subject to time-dependent perturbing field(s), expressed as operators V^{ω} at frequency ω, as

$$\begin{aligned}\langle 0(t)|A|0(t)\rangle =& \langle 0|A|0\rangle + \int_{-\infty}^{\infty} d\omega_1 e^{-i\omega_1 t}\langle\langle A; V^{\omega_1}\rangle\rangle_{\omega_1} \\ &+ \frac{1}{2}\int_{-\infty}^{\infty} d\omega_1 \int_{-\infty}^{\infty} d\omega_2 e^{-i(\omega_1+\omega_2)t}\langle\langle A; V^{\omega_1}, V^{\omega_2}\rangle\rangle_{\omega_1\omega_2} + \cdots ,\end{aligned} \tag{3.17}$$

where $|0(t)\rangle$ denotes the time-dependent wavefunction and $|0\rangle$ the unperturbed wavefunction. $\langle\langle A; V^{\omega_1}\rangle\rangle_{\omega_1}$ is a linear response function (LRF) that collects the terms to the first order in the perturbation. $\langle\langle A; V^{\omega_1}, V^{\omega_2}\rangle\rangle_{\omega_1\omega_2}$ is, correspondingly, the quadratic response function that includes the second-order terms. Higher-order responses follow in analogous manner. Response functions can be expressed in terms of spectral representations that show the connection to normal time-dependent perturbation theory [87]. For the LRF, this reads [69]

$$\langle\langle A; V^{\omega_1}\rangle\rangle_{\omega_1} = \sum_{n\neq 0}\left\{\frac{\langle 0|A|n\rangle\langle n|V^{\omega_1}|0\rangle}{\hbar\omega_1 + E_0 - E_n} - \frac{\langle 0|V^{\omega_1}|n\rangle\langle n|A|0\rangle}{-\hbar\omega_1 + E_0 - E_n}\right\}, \tag{3.18}$$

which in the case of static perturbation, $\omega = 0$, such as in normal NMR parameters and the ESR g-tensor, reduces to the sum-over-states (SOS) expression for the second-order energy correction. In general, the spectral representations of the above kind are only valid for

exact wavefunctions. In practice, approximate methods are used and the response functions are calculated by solving matrix-formed equations [87]. In the case of LRF, the response vector is calculated. It corresponds to the first-order wavefunction with respect to one of the two involved perturbation operators [69].

In the solid-state GIPAW approach, the response of the electron system to the applied static magnetic field is formulated in terms of the first-order induced current density $\mathbf{j}^{(1)}(\mathbf{r})$. This quantity is calculated via a decomposition of the individually gauge-origin-dependent diamagnetic $\mathbf{j}_d^{(1)}(\mathbf{r})$ and paramagnetic $\mathbf{j}_p^{(1)}(\mathbf{r})$ parts [85, 88], the first and second terms in

$$\mathbf{j}^{(1)}(\mathbf{r}) = -\frac{e^2}{m_e}\rho^{(0)}(\mathbf{r})\mathbf{A}_0(r) - \frac{e}{2m_e}\sum_o \langle\psi_o^{(0)}|(\mathbf{p}|\mathbf{r}\rangle\langle\mathbf{r}| + |\mathbf{r}\rangle\langle\mathbf{r}|\mathbf{p})|\psi_o^{(1)}\rangle, \tag{3.19}$$

where the summation in the second term is over all the occupied states o. The sum of the two terms above is an observable quantity that satisfies gauge invariance. Moreover, $\mathbf{j}_d^{(1)}(\mathbf{r})$ depends only on the unperturbed charge density $\rho^{(0)}(\mathbf{r})$. In contrast, $\mathbf{j}_p^{(1)}(\mathbf{r})$ involves the first-order states $|\psi_o^{(1)}\rangle$, corrected by the magnetic-field perturbation $H^{(1)} = \frac{e}{m_e}\mathbf{A_0}\cdot\mathbf{p}$, and calculated by a Green's function method [84].

3.3 Electron spin and nuclear magnetic resonance parameters

3.3.1 Molecular calculations

In molecular quantum-chemical calculations, second-order magnetic parameters, $e.g.$, $\boldsymbol{\sigma}$ and $\mathbf{J}$ are obtained by substituting the interaction operators into the standard second-order perturbation theory expression, cast in the form of a LRF [86]

$$E_0^{(2)} = H_{00}^{(2)} + \frac{1}{2}\langle\langle H^{(1)}; H^{(1)}\rangle\rangle_{\omega=0}. \tag{3.20}$$

The shielding tensor expressed via Rayleigh-Schrödinger perturbation theory, valid for closed-shell molecules, was first derived by Ramsey [89]. It consists of two parts

$$\boldsymbol{\sigma}_K = \boldsymbol{\sigma}_K^d + \boldsymbol{\sigma}_K^p, \tag{3.21}$$

where the first term refers to the diamagnetic and the second to the paramagnetic contribution. The diamagnetic term involves only the unperturbed ground state,

$$\boldsymbol{\sigma}_K^d = \frac{e^2}{2m_e}\frac{\mu_0}{4\pi}\left\langle 0\left|\sum_i \frac{\mathbf{1}(\mathbf{r}_{iO}\cdot\mathbf{r}_{iK}) - \mathbf{r}_{iO}\mathbf{r}_{iK}}{r_{iK}^3}\right|0\right\rangle. \tag{3.22}$$

The paramagnetic term involves perturbations that couple the ground-state to singlet excited states, n_S. It can be expressed as a LRF with singlet transitions

$$\boldsymbol{\sigma}_K^p = \frac{1}{\gamma_K\hbar}\langle\langle \mathbf{h}_K^{\mathrm{PSO}}; \mathbf{h}_{\mathrm{B}_0}^{\mathrm{OZ}}\rangle\rangle_{\omega=0}. \tag{3.23}$$

Here, $\mathbf{h}_{\mathrm{B}_0}^{\mathrm{OZ}}$ is the orbital Zeeman term that is linear in the external field

$$\mathbf{h}_{\mathrm{B}_0}^{\mathrm{OZ}} = \frac{e}{2m_e}\sum_i \mathbf{l}_{iO}. \tag{3.24}$$

$\mathbf{h}_K^{\mathrm{PSO}}$ is the paramagnetic nuclear spin-electron orbit term, which is one of three terms that arise from the interaction of the electrons with the nuclear magnetic moments

$$\begin{aligned}
\mathbf{h}_K^{\mathrm{PSO}} =& \frac{e\hbar}{m_e}\frac{\mu_0}{4\pi}\gamma_K \sum_i \frac{\mathbf{l}_{iK}}{r_{iK}^3} \\
\mathbf{h}_K^{\mathrm{SD}} =& \frac{e\hbar^2}{2m_e}\frac{\mu_0}{4\pi} g_{\mathrm{e}}\gamma_K \sum_i \frac{r_{iK}^2\mathbf{s}_i - 3(\mathbf{s}_i\cdot\mathbf{r}_{iK})\mathbf{r}_{iK})}{r_{iK}^5} \\
\mathbf{h}_K^{\mathrm{FC}} =& \frac{4\pi}{3}\frac{e\hbar^2}{2m_e}\frac{\mu_0}{4\pi} g_{\mathrm{e}}\gamma_K \sum_i \delta(\mathbf{r}_{iK})\mathbf{s}_i.
\end{aligned} \tag{3.25}$$

Here, the other two terms $\mathbf{h}_K^{\mathrm{FC}}$ and $\mathbf{h}_K^{\mathrm{SD}}$ are the electron spin-dependent Fermi contact (FC) and spin-dipolar (SD) terms, where $\mathbf{s}_i$ denotes the spin operator of the electron i. All of these three terms contribute to the spin-spin coupling. In the expressions above, γ_K refers to the gyromagnetic ratio of nucleus K and $\mathbf{l}_{iO/K} = -i\hbar(\mathbf{r}_i - \mathbf{R}_{O/K})\times\nabla_i$ to the angular momentum of electron i with respect to either the gauge origin, $\mathbf{R}_O$ or the location $\mathbf{R}_K$ of nucleus K.

Five physically distinct contributions appear in Ramsey's expression of the indirect spin-spin coupling tensor; $\mathbf{J}_{KL} = \mathbf{J}_{KL}^{\mathrm{DSO}} + \mathbf{J}_{KL}^{\mathrm{PSO}} + \mathbf{J}_{KL}^{\mathrm{SD}} + J_{KL}^{\mathrm{FC}}\mathbf{1} + \mathbf{J}_{KL}^{\mathrm{SD/FC}}$ [90]. Here, the first four terms contribute to the isotropic spin-spin coupling constant J and all but $J^{\mathrm{FC}}\mathbf{1}$ to the anisotropic coupling. The first is the diamagnetic nuclear spin-electron orbit (DSO) term bilinear in the nuclear spins of K and L, obtained as a ground-state expectation value of the DSO operator:

$$\mathbf{J}_{KL}^{\mathrm{DSO}} = \frac{1}{h}\langle 0|\mathbf{h}_{KL}^{\mathrm{DSO}}|0\rangle, \tag{3.26}$$

where

$$\mathbf{h}_{KL}^{\mathrm{DSO}} = \frac{e^2\hbar}{2m_e}\left(\frac{\mu_0}{4\pi}\right)^2\gamma_K\gamma_L\sum_i \frac{(\mathbf{r}_{iK}\cdot\mathbf{r}_{iL})\mathbf{1} - \mathbf{r}_{iL}\mathbf{r}_{iK}}{r_{iK}^3 r_{iL}^3}. \tag{3.27}$$

The second term, $\mathbf{J}_{KL}^{\mathrm{PSO}}$, is a second-order contribution that involves perturbations that couple to singlet excited states. In contrast, the last three terms include triplet perturbations, the isotropic FC term and the SD term, as well as the anisotropic SD/FC cross-term of the two [28, 91]. All these contributions can be calculated from the linear response functions

$$\mathbf{J}_{KL}^{\mathrm{PSO}} = \frac{1}{h}\langle\langle 0|\mathbf{h}_K^{\mathrm{PSO}}; \mathbf{h}_L^{\mathrm{PSO}}|0\rangle\rangle_{\omega=0}, \tag{3.28}$$

$$\mathbf{J}_{KL}^{\mathrm{SD}} = \frac{1}{h}\langle\langle 0|\mathbf{h}_K^{\mathrm{SD}}; \mathbf{h}_L^{\mathrm{SD}}|0\rangle\rangle_{\omega=0}, \tag{3.29}$$

$$\mathbf{J}_{KL}^{\mathrm{FC}} = \frac{1}{h}\langle\langle 0|\mathbf{h}_K^{\mathrm{FC}}; \mathbf{h}_L^{\mathrm{FC}}|0\rangle\rangle_{\omega=0}, \tag{3.30}$$

$$\mathbf{J}_{KL}^{\mathrm{SD/FC}} = \frac{1}{h}\left[\langle\langle 0|\mathbf{h}_K^{\mathrm{SD}}; \mathbf{h}_L^{\mathrm{FC}}|0\rangle\rangle_{\omega=0} + \langle\langle 0|\mathbf{h}_K^{\mathrm{FC}}; \mathbf{h}_L^{\mathrm{SD}}|0\rangle\rangle_{\omega=0}\right], \tag{3.31}$$

in which the PSO, FC, and SD operators are given in (3.25).

The EFG tensor is a ground-state property. It is sensitive to the electron density near the nucleus and is defined as a sum of the nuclear contribution and an expectation value:

$$\mathbf{V}_K = \frac{e}{4\pi\epsilon_0}\left[\sum_{K\neq L} Z_L \frac{3\mathbf{R}_{KL}\mathbf{R}_{KL} - \mathbf{1}R_{KL}^2}{R_{KL}^5} - \langle 0|\sum_i \frac{3\mathbf{r}_{iK}\mathbf{r}_{iK} - \mathbf{1}r_{iK}^2}{r_{iK}^5}|0\rangle\right]. \quad (3.32)$$

3.3.2 Solid-state calculations

The solid-state magnetic property calculations presented in this thesis are carried out by the GIPAW approach [85]. The GIPAW shielding calculation is based on the fact that the contributions arising from the core electrons are largely independent of the chemical environment [92]. The GIPAW shielding tensor is formulated as the sum [93]

$$\boldsymbol{\sigma} = \sigma_{\text{core}}\mathbf{1} + \boldsymbol{\sigma}_{\Delta d} + \boldsymbol{\sigma}_{\Delta p} + \boldsymbol{\sigma}_{\text{bare}}, \quad (3.33)$$

where the first term σ_{core} is the isotropic, system-independent, core contribution. It can be obtained from the Lamb formula [31, 94] by setting the gauge origin to the nucleus [61]. The three latter terms arise from the current response. Inside the GIPAW core region, the differences of the all-electron and pseudo-valence currents, $\mathbf{j}_{\Delta p}$ and $\mathbf{j}_{\Delta d}$, induce the paramagnetic and diamagnetic correction fields $\mathbf{B}_{\Delta p}$ and $\mathbf{B}_{\Delta d}$, which can be obtained separately from the linear Biot-Savart law

$$\mathbf{B}_{\text{ind}}(\mathbf{r}_K) = \frac{\mu_0}{4\pi}\int \mathbf{j}^{(1)}(\mathbf{r}) \times \frac{\mathbf{r}_K - \mathbf{r}}{|\mathbf{r}_K - \mathbf{r}|^3}\, d\mathbf{r}, \quad (3.34)$$

where the induced current density is decomposed into three parts, $\mathbf{j}^{(1)}(\mathbf{r}) = \mathbf{j}^{(1)}_{\Delta p} + \mathbf{j}^{(1)}_{\Delta d} + \mathbf{j}^{(1)}_{\text{bare}}$. Outside the core region, the all-electron and pseudo-partial waves are identical, and these corrections vanish. Therefore, the contribution of the induced field from outside of the core region can be calculated from the current resulting from the perturbed pseudo-wavefunction, $\mathbf{j}^{(1)}_{\text{bare}}$. The resulting field, $\mathbf{B}_{\text{bare}}$, is unphysical on its own, but together with the corrections, the induced field corresponding to the all-electron situation is obtained. Furthermore, the corresponding shielding contributions are obtained from (2.2) giving, together with the core contribution, the all-electron shielding tensor [85].

In the plane-wave-pseudopotential approach, the components of the EFG tensor, $\mathbf{V}_K$, can be calculated from the total charge density $n(\mathbf{r})$ [61]

$$V_{K,\epsilon\tau} = \int \frac{n(\mathbf{r})}{|\mathbf{r} - \mathbf{R}_K|^3}\left[\delta_{\epsilon\tau} - 3\frac{(r_\epsilon - R_{K,\epsilon})(r_\tau - R_{K,\tau})}{|\mathbf{r} - \mathbf{R}_K|^2}\right] d\mathbf{r}, \quad (3.35)$$

where $n(\mathbf{r})$ consists of a sum of three terms arising from ionic charges, pseudised valence charge density, and the PAW correction that takes into account the deviation of the pseudo- and all-electron charge densities at the atomic site. Hence, there are three distinct corresponding contributions to EFG [95].

Based on the GIPAW ansatz [85], an expression for the g-tensor due to the induced electronic currents within the formalism of spin-polarised DFT[§], was provided by Pickard and Mauri [96]. They formulated the g-tensor as

$$\mathbf{g} = g_{\mathrm{e}}\mathbf{1} + \mathbf{\Delta g}_{\text{Z-KE}} + \mathbf{\Delta g}_{\text{SO}} + \mathbf{\Delta g}_{\text{SOO}}. \tag{3.36}$$

Here the corrections to the free-electron g-factor, g_e, arise from the energy terms that are bilinear in the electron spin and the external magnetic field $\mathbf{B}_0$, according to equation (2.13) [18, 19]. $\Delta\mathbf{g}_{\text{Z-KE}}$ is the Zeeman kinetic energy correction arising from a bilinear operator in these two variables. $\Delta\mathbf{g}_{\text{SO}}$ is the second-order spin-orbit (SO) term, where the spin of the unpaired electron interacts with its own orbital motion affected, in turn, also by the orbital Zeeman interaction with $\mathbf{B}_0$. Respectively, $\Delta\mathbf{g}_{\text{SOO}}$ is the 2-electron spin-other-orbit (SOO) term that describes the relative motion of the other electron with respect to the nuclear frame. The largest correction comes from the $\mathbf{g}_{\text{SO}}$-term that, in turn, depends on the Kohn-Sham potential and electronic currents induced by $\mathbf{B}_0$ onto the majority and minority spin channels. The role of the GIPAW approach is to obtain an accurate description of the all-electron currents in the core regions, where the KS-potential diverges at the nucleus site. In a manner similar to that described above for the GIPAW shielding tensor, the SO-contribution to the g-tensor is calculated in three different parts: $\Delta\mathbf{g}_{\text{SO}}^{\text{bare}}$, $\Delta\mathbf{g}_{\text{SO}}^{\Delta d}$, and $\Delta\mathbf{g}_{\text{SO}}^{\Delta p}$. The first two, so-called pseudo-valence and diamagnetic terms can be evaluated from the PAW-corrected ground-state pseudo-wavefunctions. In contrast, the paramagnetic correction term is more involved and requires first-order linear response wavefunctions. The $\Delta\mathbf{g}_{\text{Z-KE}}$ correction depends only on the kinetic energies of the majority and minority spin channels. It can be determined straightforwardly from the PAW-corrected ground-state wavefunction. As compared to the SO-term, only a small contribution arises from the SOO-term, which depends on the induced field and the spin density of the channels. Since neither of these quantities diverge at the nucleus and the obtained corrections are minor, no large error is made when the SOO-correction is obtained by evaluating the induced field arising due to the $\mathbf{j}_{\text{bare}}^{(1)}$ and the pseudo-valence spin density alone [96].

Magnetic hyperfine parameters arise from the interaction of the nuclear magnetic moment and electron spin density. The isotropic HFC component arises from the expectation value of the FC interaction (3.25) [18], which is only sensitive to the s-electron density located at the nucleus. Instead, the anisotropic component is expectation value of the SD term (3.25), having sensitivity particularly to the p-electron contribution to the density in the close vicinity to the nucleus. A pseudopotential-plane-wave calculation method for HFC was introduced by Van de Walle and Blöchl [97, 98], based on the pure PAW spin density. What is excluded from the, otherwise highly accurate frozen-core PAW wavefunction, is the effect of the spin polarisation of the core states [99, 100]. This effect may contribute significantly to the s-type density at the nucleus. Furthermore, spin polarisation contributes mainly in systems where the unpaired spin populates other than s-type atomic orbitals. While the effect only has a small influence on the dipolar part, the incorrect spin density at the nucleus leads to unreliable contact values.

In the studies of point-defected paramagnetic graphenes included in the thesis, HFCs are

[§]Spin-polarised DFT deals with systems containing unpaired electrons, and concerns the KS equations separately for spin-up and spin-down electrons, which are sometimes referred as spin channels. Hence, both the electron density and the spin density are fundamental quantities. The total charge density is the sum of the spin-up and spin-down electron densities, $n_\uparrow + n_\downarrow$, the net spin density being their difference $n_\uparrow - n_\downarrow$ [45].

reported for the first-row carbon atom. In this case, the spin-polarisation effect originates from the $1s$ core shell. In the present study this has been included by the perturbative core-level polarisation (PCLP) [100] method. First, the frozen-core all-electron wavefunction in the core region is obtained by the PAW approach. Secondly, the local spin density and charge potential are evaluated from the reconstructed all-electron wavefunction. Finally, the potential is used to estimate the spin-polarised core levels by means of first-order perturbation theory.

3.4 Faraday optical rotation parameters

The magneto-optic rotation angle Φ, per unit of optical path length l, can be written as [40, 41]

$$\frac{\Phi}{l} = \frac{1}{2}\omega\mathcal{N}\mu_0 c\,\mathrm{Im}\langle\alpha'_{XY}\rangle, \tag{3.37}$$

when the magnetic field is in the direction (Z) of the beam. Here, $\mathcal{N}$ refers to the number density either of the molecules in the case of FOR, or to that of the nuclei K in the NSOR case. The conventional dynamic polarisability can be expressed as a LRF $\boldsymbol{\alpha}(\omega) = -\langle\langle\boldsymbol{\mu};\boldsymbol{\mu}\rangle\rangle_\omega$, which is modified, in the case of FOR and NSOR, by the static perturbation caused by $\mathbf{B}_0$ or $\mathbf{I}_K$, respectively. In other words, the Verdet constant V is proportional to the derivative of antisymmetric polarisability $\boldsymbol{\alpha}'^{(B_0)}(\omega)$ with respect to $\mathbf{B}_0$ and, respectively, the constant V_K is proportional to the derivative of $\boldsymbol{\alpha}'^{(K)}(\omega)$ with respect to $\mathbf{I}_K$. Hence, both magneto-optical rotation constants can be calculated, in the case of closed-shell molecules, by third-order time-dependent perturbation theory as the quadratic response functions [86, 101]

$$\begin{aligned} V(\omega) &\propto \omega\epsilon_{\epsilon\tau\nu}\left\langle\left\langle\mu_\epsilon;\mu_\tau,h^{\mathrm{OZ}}_{\mathrm{B}_0}\right\rangle\right\rangle_{\omega,0} \\ V_K(\omega) &\propto \omega\epsilon_{\epsilon\tau\nu}\left\langle\left\langle\mu_\epsilon;\mu_\tau,h^{\mathrm{PSO}}_{K,\nu}\right\rangle\right\rangle_{\omega,0} \end{aligned}, \tag{3.38}$$

where μ_ϵ and μ_τ are the components of the electric dipole moment. The third interaction is a static magnetic operator that characterises the OZ-interaction (equation 3.24) with the external field or the orbital hyperfine (PSO) interaction (equation 3.25). With the definition of the FOR angle (equation 2.23) the Verdet constant can be expressed as

$$V = -\frac{1}{2}\omega\mathcal{N}\mu_0 c\frac{e^3}{2m_e}\frac{1}{6}\sum_{\epsilon\tau\nu}\epsilon_{\epsilon\tau\nu}\mathrm{Im}\langle\langle r_\epsilon;r_\tau,l_{O,\nu}\rangle\rangle_{\omega,0}, \tag{3.39}$$

in the unit of rad/(T m) [25]. Denoting the degree of nuclear spin polarisation along the beam as $P_K = \langle I_{K,Z}\rangle/I_K$, the NSOR angle $\Phi^{(K)}_{\mathrm{NSOR}}$ per unit of optical path length, spin polarisation, and molar concentration $n_K = \mathcal{N}/N_A$ (N_A is Avogadro's constant) of the polarised nuclei K, becomes [43]

$$V_K = \frac{\Phi^{(K)}_{\mathrm{NSOR}}}{lP_K n_K} = -\frac{1}{2}\omega N_A c I_K\frac{e^3\hbar}{m_e}\frac{\mu_0^2}{4\pi}\gamma_K\frac{1}{6}\sum_{\epsilon\tau\nu}\epsilon_{\epsilon\tau\nu}\mathrm{Im}\left\langle\left\langle r_\epsilon;r_\tau,\frac{l_{K,\nu}}{r_K^3}\right\rangle\right\rangle_{\omega,0}. \tag{3.40}$$

The experimentally convenient unit for V_K is 10^{-6} rad/(M cm). The expressions (3.39) and (3.40) lend themselves to quantum-chemical calculation of the components of the polarisability derivatives $\alpha'_{\epsilon\tau,\nu}$ in the molecule-fixed frame.

4 Review of papers

4.1 NMR: Large-system limit and spectral patterns of finite fragments

For the characterisation of large 2D-crystals of graphene and their derivatives, NMR spectroscopy may provide hitherto unused potential. NMR can provide information of the local structure and composition, which may be difficult to obtain otherwise [102, 103]. Paper I tackles this issue by providing predictions of NMR parameters for large graphene systems, as well as the hydrogenated and fluorinated derivatives, graphane and fluorographene, respectively. The total organic synthesis from precursors is one way of manufacturing uniform graphenes. Actually, large benzene-based macromolecules have been produced for some time already [11, 12, 104]. Due to their structural similarities with graphene, they have many of the characteristics of 2D graphene sheets [11, 12]. In addition, they feature both edge and quantum confinement effects and are, thus, also called graphene quantum dots (GQDs) [13]. GQDs are at the center of significant research effort due to their size-tunable properties such as fluorescence [14] and plasmon effects [105–107]. Hence, GQDs and their chemical derivatives are candidate device materials for future electronic and optical applications [11, 12, 106]. In this context, NMR could provide useful additional information. Therefore, theoretical investigations of the NMR spectral patterns can be of use in confirming the experimental findings on the synthesised structures, $e.g.$ concerning their specific size and composition. Motivated by the lack of both theoretical and experimental NMR data on sp^2-hybridised hydrocarbon flakes, we carried out a theoretical investigation of the characteristic spectral patterns, of these specifically finite-size systems in Paper II.

In Paper I, two different DFT methods were applied. The quantum-chemical cluster approach was exploited for hexagonal graphene flakes of growing size. This was done to extrapolate the NMR parameters for the innermost part of system to the large-system limit, which is the representative situation for the innermost region of large graphene flakes. The results turned out to rapidly converge to limiting values. These values were compared to the results obtained by solid-state calculations, which dealt, due to the periodic boundary conditions used, directly with extended systems.

Two different finite quantum-chemical models of increasing size were used, referred to as 'relaxed' and 'fixed', respectively. In the fixed models, the structure of the flakes

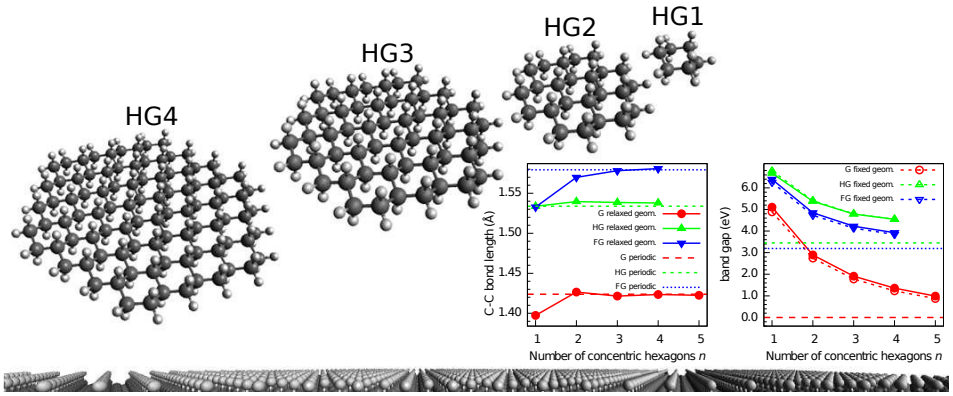

Figure 4.1. Increasing-size graphane flakes and part of the extended graphane layer (bottom) are illustrated. On the right, quantum-chemical (PBE/co-r) and periodic results for the innermost CC bond length (Å) and band gap (eV) for finite graphene (Gn), graphane (HGn) and fluorographene (FGn) models with increasing number n of concentric hexagonal rings.

consisting of concentric hexagons with zigzag perimeter corresponded to the optimised periodic structure. In the relaxed models, the molecular structures were independently optimised for each specific system size. In both model types, the perimeter carbon atoms were hydrogen-terminated with optimised positions. Figure 4.1 illustrates increasing-size graphane flakes. The figure also reveals the convergence of the geometry of the innermost part of the relaxed models toward the periodic situation, although the energy gap between the HOMO and LUMO orbitals is not even nearly settled at these system sizes. For both the first- ($\boldsymbol{\chi}_{^2\mathrm{H}}$) and second-order ($\boldsymbol{\sigma}$, $\boldsymbol{J}$) NMR properties the convergence was nevertheless obtained due to the local nature of the magnetic perturbations involved. This can be understood as being due to the trends in the decreasing excitation energy denominators in the second-order properties becoming overcompensated by the trends in the matrix elements of the local perturbation operators, present in the nominators of the second-order expressions.

The comparison of NMR parameters obtained by solid-state and quantum-chemical approaches is only feasible when the basis sets used are of comparable accuracy and, furthermore, the same DFT functional should be used. For that reason all the presently investigated periodic systems were carefully tested against computational choices such as the adequacy of k-sampling and cut-off energy. The corresponding task for the quantum-chemical NMR calculations of increasing-size clusters is demanding, as the basis set should remain of feasible size for properties in systems of very different sizes. This issue was solved by using completeness-optimised (co) basis sets [70], developed for this purpose in Paper I, and named as co-NMR-r. Also the locally dense basis set method [108] was used, where the innermost region of the clusters (for which the NMR parameters were calculated) was represented by a well-saturated basis, whereas a lower-level basis covered the remaining part. The PBE functional was used in both approaches.

The main result that all studied systems (G, HG and FG) share, is the ^{13}C chemical shift

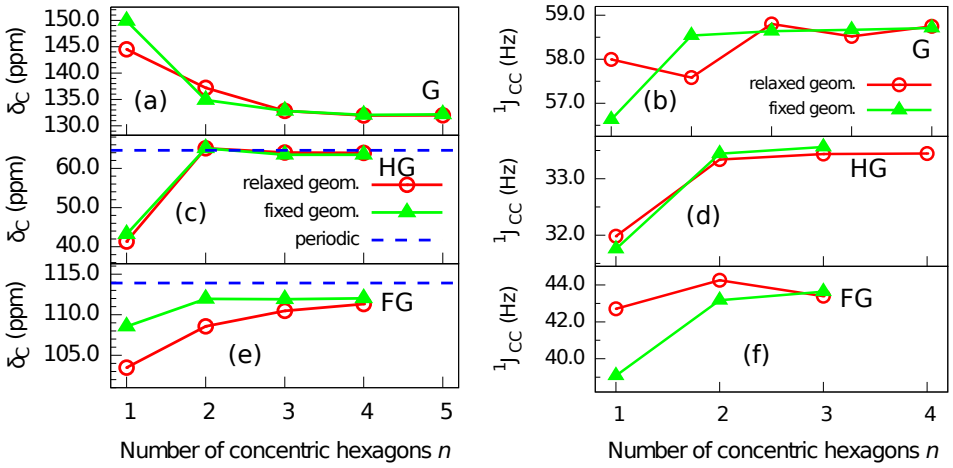

Figure 4.2. Innermost ^{13}C NMR chemical shifts (δ) and one-bond ^{13}C^{13}C indirect spin-spin coupling constants (J) for finite models of (ab) graphene (Gn), (cd) graphane (HGn), and (ef) fluorographene (FGn), as functions of the number n of concentric hexagonal rings. For HG and FG, also the periodic δ results are given.

δ_{C} (illustrated in Figure 4.2), which in the three types of environment obtains distinct values. In the case of periodic calculations of G it was impossible to apply perturbation theory to obtain converged results for $\boldsymbol{\sigma}_{\mathrm{C}}$, due to the vanishing band gap. Thus, the cluster method offered presently the only way to obtain converged first-principles NMR predictions for G. $\boldsymbol{\sigma}$ was calculated for the Gn models up to G5. The relaxed geometry of the innermost ring converges to the periodic structure at G4. At that model size, the δ_{C} results appropriate to both the relaxed and fixed geometries converge to the same value. The shielding and coupling anisotropies are also consistent at both geometries (Paper I).

In contrast, the sp^3-hybridised HG and FG systems have a clear, finite band gap, which offers the possibility to compare δ_{C} results with those obtained in the finite, quantum-chemically calculated flakes. In the case of HG, both δ_{C} and $\Delta\sigma_{\mathrm{C}}$ values for the flakes, both in their relaxed and fixed geometries, converge from HG3 onward to practically the same periodic result. In the case of FG, δ_{C} corresponding to the fixed-geometry clusters stabilises already at the model size FG2. In the optimised clusters, structural relaxation in the core region occurs slowly as a function of n (Figure 4.1) and the fixed-geometry result is only reached at FG4. Notably, the converged quantum-chemical results for both carbon and fluorine (shown in Paper I) converge to values ca. 2 ppm below the corresponding periodic shifts. A similar difference was obtained also for δ_{F}; the periodic result equals 114 ppm while 110 ppm was obtained for the converged fixed-geometry in size FG3. In HG, the δ_{H} value is small, as 0.5 ppm was obtained in both the periodic and cluster approaches. CH_4 was the reference compound for δ_{C} and δ_{H}, while CH_3F was used for δ_{F}. The deuterium ^{2}H quadrupole coupling in graphane clusters converged to 168 kHz at the G2 size for fixed models, while 167 kHz was obtained for relaxed models at size G3 onward. In contrast to these values, 172 kHz was obtained in the solid-state calculation. These calculations

showed that the property requires flexibility from the basis set. The reason for the existing difference between values obtained by the present two computational approaches remains unclear, however.

Figure 4.2 illustrates also the convergence of the one-bond J_{CC} coupling constant between ^{13}C nuclei in the innermost hexagonal ring of the flakes. In general, the fixed-geometry cluster results for J converge at $n = 2$, faster than for δ. Hence, fixed-geometry cluster calculations can be used to predict J with moderately small model sizes. Comparing the three different systems, $^1J_{\mathrm{CC}}$ changes between G (sp^2) and HG (sp^3) qualitatively similarly to the situation in small hydrocarbons [109], with the FG result in-between. The two-bond J_{CC} coupling constants are small, close to zero in all systems. In contrast, the three-bond coupling constant converges to the value of 6 Hz for G systems while for FG and HG, corresponding limits are 2 and 1 Hz, respectively.

Disregarding the systematic errors due to the use of DFT, the predicted chemical shifts for experimental purposes are (in ppm), $\delta_{\mathrm{C}} = 132$ (G), 63 (HG), and 112 (FG), as well as $\delta_{\mathrm{H}} = 1$ (HG) and $\delta_{\mathrm{F}} = 120$ (FG). The experimental ^{13}C shifts of G sheets, converted to the methane reference, are in the range 122.6–127.6 ppm [110–113] . DFT has the tendency of systematic deshielding (*i.e.*, overestimating shift) as compared to accurate ab initio results [91], which was observed also in the DFT calibration tests carried out in the present study. Comparing with typical ^{13}C shift in graphite compounds [114] the predicted shifts for G and HG indeed fall into the region of graphitic carbon. In contrast, the carbon nucleus is less shielded in FG than in the fluorinated 3D graphite [114, 115]. The spin-spin coupling predictions are (in Hz) for G, HG, and FG in this order: $^1J_{\mathrm{CC}} = 59$, 34, and 44, $^2J_{\mathrm{CC}} = 0$, -1, and 0, $^3J_{\mathrm{CC}} = 6$, 1, and 2, $^1J_{\mathrm{CH}} = 127$ and $^{3/4}J_{\mathrm{HH}} = 12/0$ (HG), $^1J_{\mathrm{CF}} = 325$, as well as $^{3/4}J_{\mathrm{FF}} = -10/31$ (FG). Due to the large error expected for $^1J_{\mathrm{CF}}$ by DFT [116], that particular value is given for completeness only. In conclusion, the predictions of the NMR parameters presented in Paper I concern the G, HG and FG systems in their bulk- and large-system limit. Therefore, the focus of the cluster calculations was restricted only to the centermost nuclei of the flakes, corresponding to that desired condition.

The results obtained with the two different geometry types, relaxed and fixed, converged to practically the same limiting values. Hence, as a methodological prospect, one can use the fixed-geometry cluster approach for obtaining the NMR parameters of extended 2D systems with moderately small model size. The present work illustrates that this approach is plausible and it, in particular, enables obtaining the parameter values of extended 2D systems with a vanishing band gap.

In Paper II, carbon-13 NMR chemical shifts were calculated particularly for the finite flakes. We focused on the qualitative trends of the spectral patterns predicted for increasing-size fragments of graphene, but also its graphane and fluorographene counterparts. Both crenelated (armchair boundary) and concentric hexagon-shaped (zigzag) fragments were investigated, to gain information of the effect of different types of flake boundaries. Continuous spectral lines were obtained from the calculated chemical shifts by applying a Lorentzian broadening. The B3LYP variant of DFT was used and the requirement of converged basis set for chemical shifts was fullfilled by using the co basis (Paper I) to cover whole flake in each case.

In Figures 4.3 and 4.4, the calculated ^{13}C NMR chemical shift stick spectra of increasing-size crenelated and concentric fragments of the sp^2-hybridised graphene, are shown. The perimeter nuclei of the two systems have apparently different chemical shifts. The spectra

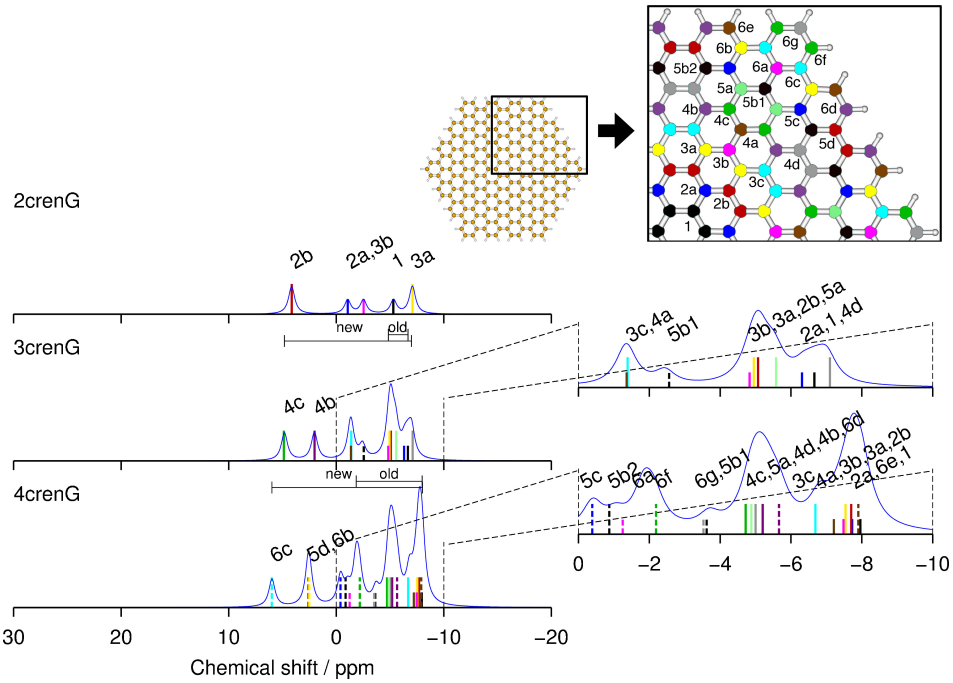

Figure 4.3. Calculated (B3LYP/co-NMR-r) carbon-13 NMR chemical shift stick spectra for finite crenelated graphene fragments of increasing size with armchair boundary ($m$crenG, $m = 2-4$). Each signal is given with its own unique colour, line style, and label as presented in the inset. The "new" lines denote the result of adding the outermost atomic layer, whereas the "old" lines arise from nuclei that reside in the inner hexagonal shells. The structural fragments in the top right corner serve to identify the lines with color encoding. The zero of the chemical shift scale has been chosen at the signal of G1 (benzene).

in Figure 4.3, are for the increasing-size armchair fragments, acronymed here as $m$crenG where m indicates the system size. The spectra feature an almost constant characteristic spread with increasing m. In contrast, the spectra of zigzag fragments in Figure 4.4, acronymed as Gn, show a widening chemical shift range with increasing n. In both kinds of systems, carbon-13 signals coming from the inner part of the fragment move systematically to the right-hand side of the spectrum, $i.e.$, they become more shielded when a new concentric ring is added. The widening of the spectra in the case of Gn system arises from the perimeter nuclei that become less and less shielded with increasing system size, forming a sparse high-shift spectral region. In contrast, in the $m$crenG systems, the signals introduced by the most recently added carbon layers appear both to the left and to the right (bigger and smaller shifts, respectively) from the broad band of signals arising from the nuclei in the inner region. Moreover, in the Gn systems, these inner nuclei form a denser and more intense band than in the $m$crenG systems. This apparently results from the larger, uniform graphene-like chemical environment appearing in Gn, as compared to

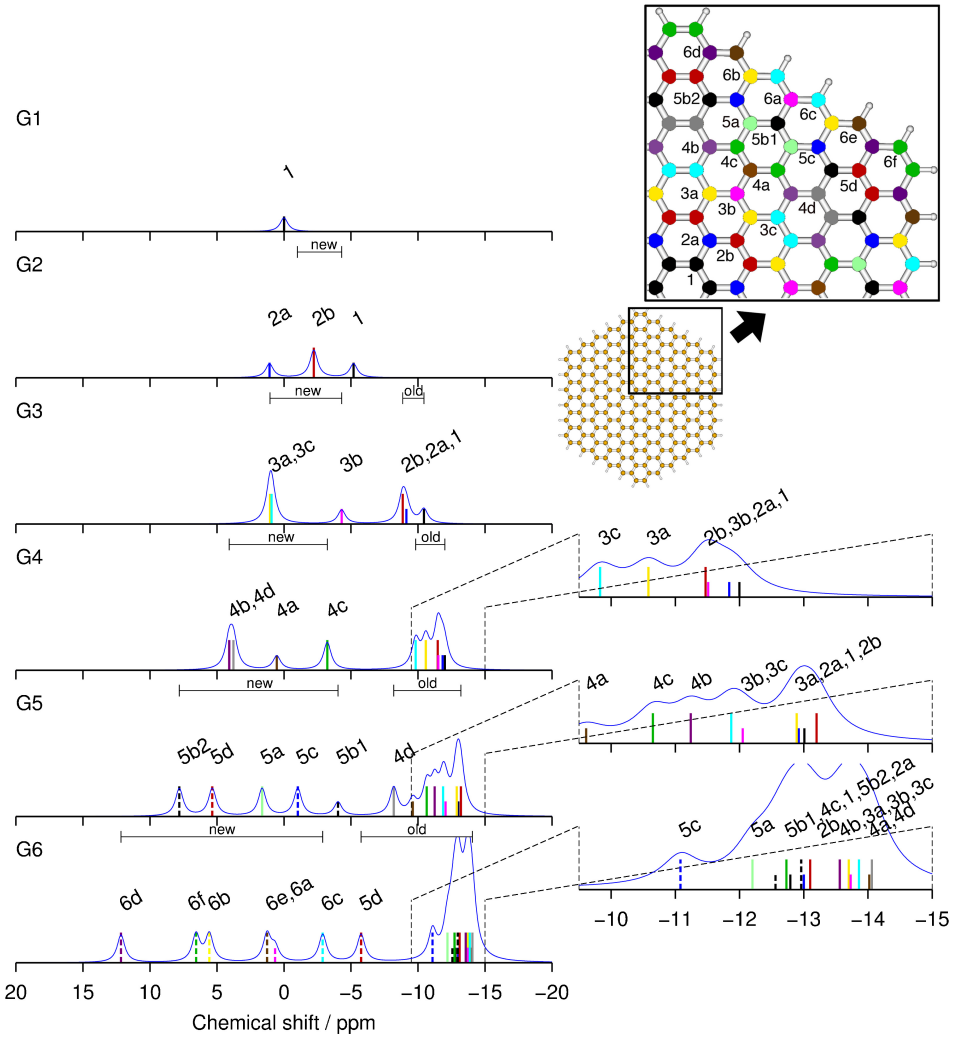

Figure 4.4. As Figure 4.3, but for the graphene fragments of increasing size with zigzag boundary (Gn, $n = 1-6$).

systems of corresponding size with armchair boundary.

The corresponding spectra for hydrogenated graphene fragments, HGn with zigzag boundary and $m$crenHG (armchair) (Figures 6-7 in Paper II), collectively differ from those of the pure sp^2-systems. Signals arising from the interior part of these sp^3-hybridised fragments are now packing to the left-hand side of the spectrum, at large shift values. Their behaviour is, hence, totally the opposite to that of the graphenic fragments. Additionally, these interior signals are roughly 80 ppm less shielded in the hydrogenated systems. The spectra of the graphane flakes are mutually overall similar, possessing a fairly stable

characteristic band of "old" signals in systems of increasing size. The only remarkable difference comes from the signals of the perimeter nuclei. In the HGn systems these "new" signals have the smallest shift values and appear to the right of the interior signals. In the $m$crenHG flakes, however, some perimeter nuclei give the highest shifts, and appear to the left of the interior signals. A similar behaviour to that described here for the hydrogenated graphene fragments, occurs also in the other studied sp^3-systems, fluorographene flakes. Their calculated spectra are illustrated in Figures 8-9 of Paper II.

The reasons for nuclei in some systems becoming less and in the others more shielded, was rationalised in Paper II with the aid of the paramagnetic shielding expression (Eq. 3.23) that, jointly with the diamagnetic contribution, constitute the total observable shielding. This kind of division is in principle arbitrary (it depends on the chosen gauge for the vector potential) and indeed the sum was directly obtained by the GIAO technique in the present production calculations. In practice, the separated paramagnetic term offers an analysis tool for the chemical shift trends. That is because the diamagnetic term, with a reasonable choice of the gauge origin, contains only information of the electron density close to the nucleus due to the ground-state nature of this term. It is the paramagnetic part that is mainly responsible for the chemical shift trends between different systems. To be precise, this analysis is based both the inverse dependence of σ^p on the excitation energies and the direct dependence on the magnetic matrix elements of the operators (shown in equation 3 of Paper II). Thus, in order for a nucleus to be less shielded than others, the "short-sighted", localised PSO (orbital hyperfine) operator requires a bigger amplitude of the excited state at precisely that nuclear site.

Figure 4.5 illustrates the localisation and the amplitude of the excitation via the difference density between the second (first) excited state and the ground state of the G2 (HG2) fragment. The symmetry species of these states correspond to the in-plane component of the shielding tensor. The figure exemplifies the findings on the trends in the chemical shifts

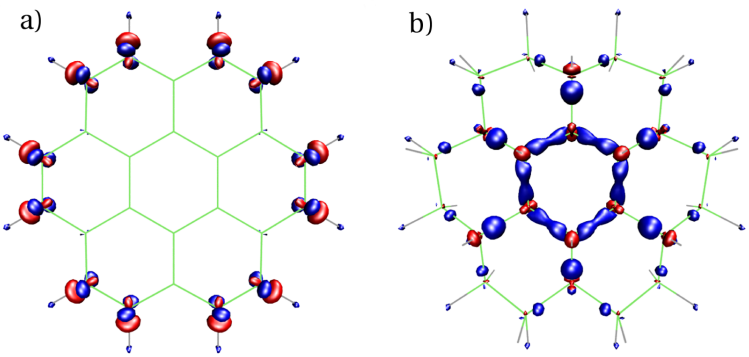

Figure 4.5. Calculated difference density a) between the second excited state and the ground state in the E_{1g} irrep (irreducible representation of the D_{6h} point group, in which h_x^{PSO} and h_y^{PSO} operate) for G2 and b) between the first excited state and the ground state in the E_g irrep (where h_x^{PSO}, and h_y^{PSO} operate in the D_{3d} point group) for HG2.

of the studied graphene flakes. An efficient coupling of the electronic ground state to the accessible excited states by (particularly) the localised hyperfine operator, causes a bigger (more negative) paramagnetic contribution and, consequently, a smaller shielding. In the present graphene systems, this coupling becomes progressively smaller for the inner atoms of the fragments upon increasing the system size. Instead, the symmetry-allowed, low-lying excitations occur at the perimeter of graphene flakes as illustrated in Figure 4.5(a). In contrast, as Figure 4.5(b) depicts, a strong coupling to the excited states persists for the inner carbon sites of the chemically functionalised graphenes, which causes a smaller shielding and, thus, a bigger chemical shift in the inner regions of the sp^3-hybridised graphene flakes. The packing of the peaks to the right (left) of the chemical shift spectrum for graphene flakes (graphane and fluorographene) results due to the localisation of the excitations, relevant for the shielding in these systems.

In general, the findings presented in Paper I should encourage NMR measurements for graphenes, by issuing starting values of the spectral parameters in the large-system limit. The calculations that were carried out in Paper II can help to understand how the properties depend on the finite size of the graphene fragments as well as their boundary structure and chemical composition. Characteristic trends were found in the ^{13}C NMR spectra. The observed spectral features do not only apply for GQDs, but should be extendable also to other types of finite-size carbon nanosystems. From the experimental point of view, the results give hope for their individual characterisation.

4.2 ESR and pNMR: Spin-1/2 defected systems

Into a uniform 2D-crystal of graphene, which is diamagnetic in its pristine form, it is possible to create local magnetic moments arising from unpaired electrons. These moments can be induced by adatoms or lattice imperfections, such as vacancies or moieties of adsorbed atoms [117, 118]. This is intensively studied both theoretically [119–126] as well as experimentally [26, 127–132] due to the technologically interesting possibility of nonmetallic magnetism. In particular, Ref. [26] reported spin-1/2 paramagnetism in a graphene sample containing fluorine adatoms. The ESR and pNMR spectroscopic methods are commonly used for structural characterisation in the development of magnetic materials. So far these methods have not been widely applied in the research on graphene magnetism, despite the fact that they have the potential to give directly measurable information of the paramagnetic defects. The purpose of Paper III was to study these spin-1/2 paramagnetic centers in graphenes in terms of ESR spectral parameters, $i.e.$, the g- and $\mathbf{A}$-tensors, as well as the pNMR nuclear shielding. These parameters can be used to quantitatively monitor the efficiency by which the unpaired spin density in conveyed to the material from the defect.

Four different defects were studied, all of which create spin-1/2 centers into the system. Two vacancy-type defects were studied in the sp^3-hybridised graphane and fluorographene systems, acronymed here as V_H@HG and V_F@FG. In these two models, a hydrogen or fluorine atom is missing, respectively. Furthermore, two defects were studied in the sp^2-hybridised graphene, consisting of hydrogen and fluorine adatoms, denoted H@G and F@G. The calculations were based on periodic boundary conditions with supercells

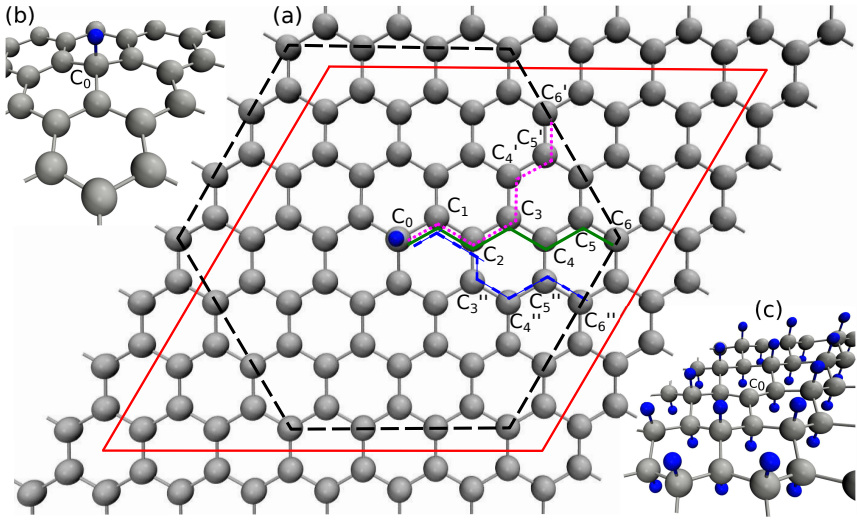

Figure 4.6. (a) Optimised structure of an H adatom-induced defect in a 6×6 unit cell of graphene. The supercell is shown with full lines and the corresponding Voronoi cell by the dashed lines. Symmetry-independent ^{13}C sites are labelled with numbers increasing from the carbon site with the adatom (C_0). ESR hyperfine couplings and pNMR shieldings are reported for the nuclei C_i along the solid green bonding path. The inset (b) highlights the region with H or F adatom in the sp^2-hybridised graphene sheet (H@G and F@G), whereas in the inset (c), the vacancy-type defect in hydrogenated/fluorinated sp^3-hybridised graphene (V_H@HG and V_F@FG), is illustrated.

containing one defect center. Specifically $n \times n$ supercell sizes were used, with $n = 3, 6, 9,$ and 12. n stands for the number of complete carbon hexagons confined in the supercell. The supercells of different sizes enabled considering the convergence of the ESR and pNMR parameters with the system size. Figure 4.6 illustrates the supercell of the size of 6×6.

In the sp^3-hybridised systems V_F@FG and V_H@HG, the defect is very localised and hosts spin density only at the closest atoms, as shown in Figure 4.7(a). These systems possess a large majority spin density at the sp^2-hybridised carbon C_0 of the vacancy, while the next-neighbour atom (C_1) houses some minority spin density. Due to this reason, both systems have enhanced ESR parameters and, consequently, also pNMR shielding values, only in the vicinity of the defect. In the case of V_H@HG, the g-values as well as the isotropic and anisotropic HFC contributions (the Fermi contact and dipolar hyperfine coupling) converge to values independent of the supercell size already at the smallest 3×3 system, implying non-interacting paramagnetic centers at the corresponding separation of defects. A remarkable high value of 160 MHz was obtained for the isotropic HFC at C_0, with a decay to zero value within 3 CC bonds from the defect center. For the V_F@FG system, largely the same was observed, apart from the fact that convergence was reached at the larger 6×6 system size, illustrated in Figure 4.8. Both systems feature monotonically decaying dipolar contribution, with a value of 150 MHz only at the C_0 atom.

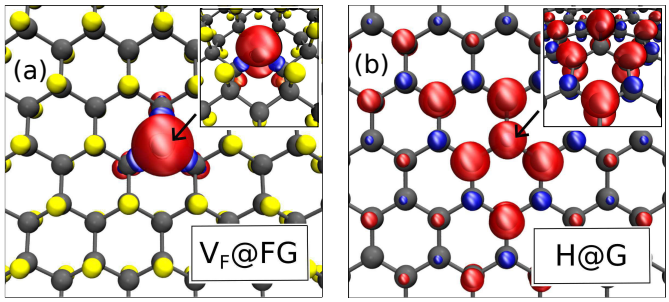

Figure 4.7. Spin densities of models for (a) fluorine vacancy in fluorographene (V_F@FG) and (b) hydrogen adatom on graphene (H@G). The arrows indicate the location of the defect. The majority (minority) spin density component is shown in red (blue) with the isosurface value of 0.02 (-0.02) $e/\text{Å}^3$.

This illustrates that almost all the p-character of the spin density is localised there.

Converged isotropic g-values (shown in Figure 3 of Paper III) of 2.00262 and 2.00253 for V_H@HG and V_F@FG, respectively, are possible to obtain by a computationally feasible k-point sampling in the sp^3-hybridised systems. In the case of V_F@FG, a large drop occurs in the g-value from the 3×3 model to the converged situation at the bigger system sizes. Similarly, the Fermi contact coupling of the 3×3 system deviates from the converged value that is obtained at both the two larger V_F@FG system sizes. This indicates that the 3×3 model is too small to present non-interacting vacancies. Figure 4.8 illustrates also that the ^{13}C pNMR shielding constant is greatly magnified for the C_0 and C_1 nuclei.

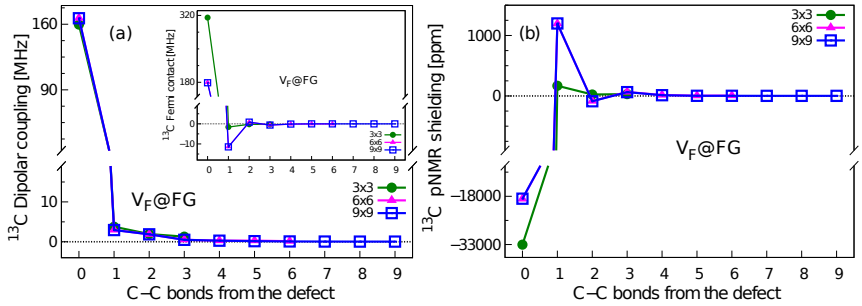

Figure 4.8. Hyperfine coupling tensor and pNMR shielding for carbon-13 nuclei as a function of the distance (number of CC-bonds) from the defect site in V_F@FG. Panel (a) depicts the anisotropic HFC constant (in MHz), *i.e.*, the dipolar coupling. It is defined as the unique principal value ($A_{33}^{\text{SD}} = A_{\perp}^{\text{SD}}$, the component perpendicular to the material plane). The inset depicts the isotropic Fermi contact contribution. In (b), the isotropic part of the pNMR shielding (in ppm) is given. The $n \times n$ configuration in the main panels refers to the different supercell sizes used.

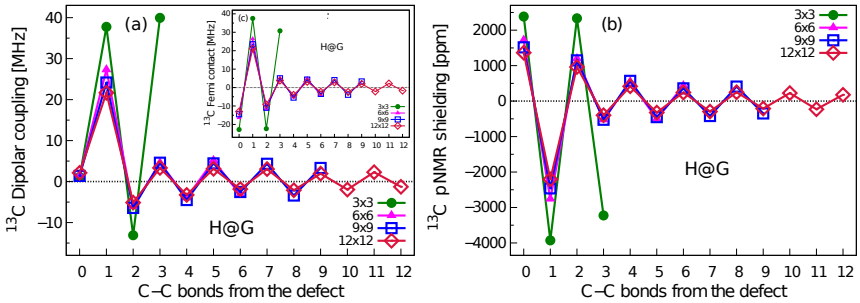

Figure 4.9. As Figure 4.8 but for the graphene model H@G hosting a single hydrogen adatom.

Similar findings, albeit with enhanced parameters ranging one CC bond further away from the defect, were observed for the V_H@HG system, as illustrated in Figure 6 of Paper III.

In contrast to the vacancy-defected systems discussed above, a long-ranged spin polarisation occurs in the adatom-defected, sp^2-hybridised graphene systems H@G and F@G, Figure 4.7(b). Therein distinct, alternating minority and majority spin densities are seen between the even- and odd-indexed nearest-neighbour atomic sites, respectively, as calculated from the defect. This phenomenon reflects the bipartite lattice, which consists of two interpenetrating hexagonal carbon sublattices, α and β and, furthermore, the fact that the defect states at the Fermi level are only formed from the p_z-orbitals on one of them [119]. In addition, in both adatom-defected graphene systems, the band gap decreases with the supercell size, approaching the situation of the zero-gap graphene. This entails difficulties to the computation of the g-tensor as a second-order property. Only for the smallest 3×3-system it was possible to obtain converged g-values, which required an extremely dense k-sampling. In contrast, the ground-state property $\mathbf{A}$ was possible to calculate for all the system sizes. Figure 4.9 shows that the defect center shows up emphasised in the Fermi contact hyperfine coupling and ^{13}C pNMR shielding, and there is a slow decay with the number of CC-bonds. Furthermore, despite the unavailability of entirely converged g-shift tensors, it was observed that the only significant contribution to the isotropic pNMR shielding constant arises from the product of the free-electron g_e factor and the isotropic Fermi contact HFC ($i.e.$, the first term in Table 2.18). The other terms contributed less than 1 ppm giving, hence, at least a partial justification for dropping off the $\mathcal{O}(\alpha^4)$ terms in the case of the two adatom systems. From Figure 4.9 it can be seen that the pNMR shielding is greatly enhanced not only in the vicinity the defect, but also further away from it, implying chances of the NMR detection.

The present study shows that a missing hydrogen and fluorine atom in graphane and fluorographene, respectively, create a spin-1/2 paramagnetic defect that has locally greatly enhanced ESR and pNMR parameters. In contrast, in graphene, the hydrogen and fluorine adatoms induce slowly decaying magnetic resonance parameters with the distance from the defect. The direct connection of these spectral parameters to the electronic structure should encourage experimental verification.

4.3 Magneto-optic rotation: Size, perimeter type and functionalisation

Ref. [133] reported an unexpectedly high Faraday optical rotation for a single layer of graphene. The rotation of the linearly polarised light in the infrared (IR) spectral region by up to 6° at 7 T external magnetic field was reported; a massive rotation to be caused by a single-atom thick material. Such a rotation holds promise of the capability of graphene as a material for fast, tunable, and ultrathin magneto-optic devices. In graphenic quantum dots, due to the quantum confinement effect, the optical transitions occur in the visible, rather than the infrared part of the electromagnetic spectrum [134, 135]. It is a well-known fact that the electronic structure of GQD systems depends crucially on the geometry of the edge region [106, 136–139], resulting in rather well-known photophysical properties [12]. Nevertheless, the Faraday rotation properties of GQDs have not been explored. In Paper IV, finite graphene flakes are studied, to reveal the dependence of FOR on the size, functionalisation by hydrogen, and perimeter structures. The possibility to gain nucleus-specific NSOR information from these systems, is also demonstrated.

The necessary quadratic response functions for V and V_K (equation 3.38) were calculated at the hybrid B3LYP [64, 65] DFT level, which has pointed out to be overall suitable for the magneto-optic properties of small carbon nanosystems [25, 140, 141]. Also in this study, the co basis-set concept [70] was used due to the rather large system sizes

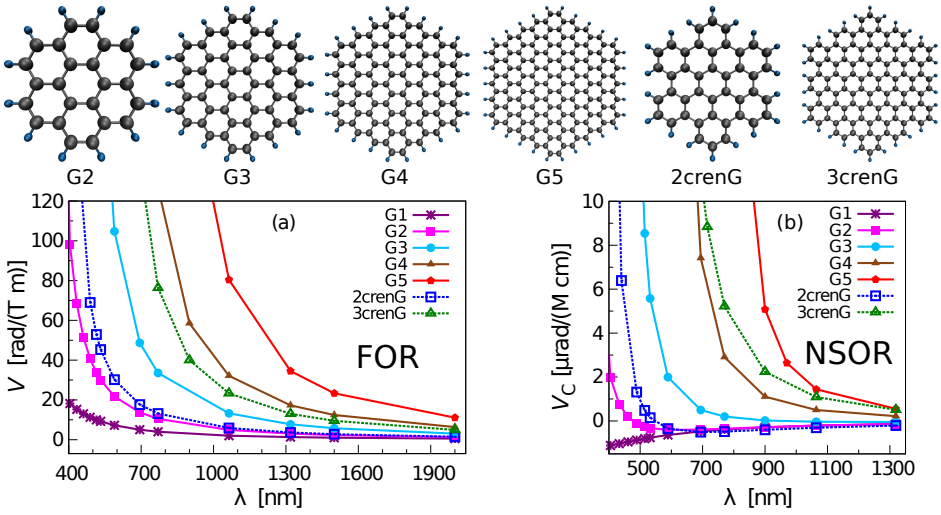

Figure 4.10. The atomic structures of the inspected finite graphene systems and their Verdet constants (V) as well as the NSOR constants V_{C} that arise from their innermost carbon nuclei. At the top, the atomic structures are illustrated for systems with zigzag (Gn, $n = 1 - 5$) and armchair ($m$crenG, $m = 2, 3$) perimeter. In panel (a), the isotropic V constants [in rad/(T m)] are plotted as functions of the light wavelength (nm) for the Gn and $m$crenG systems of increasing size. Respectively, in (b), the isotropic NSOR constants V_{C} [in μrad/(M cm)] are given for the innermost carbon nuclei.

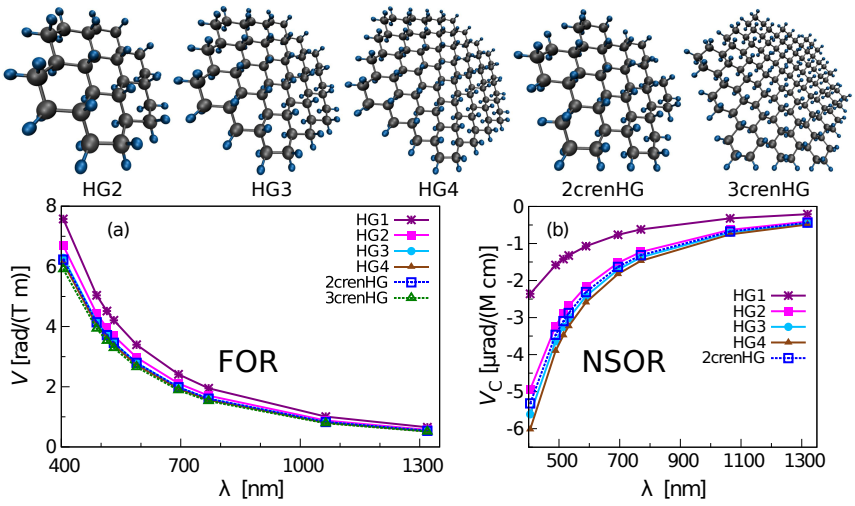

Figure 4.11. As Figure 4.10 but for graphane systems with zigzag (HGn, $n = 1 - 4$) and armchair ($m$crenHG, $m = 2 - 3$) perimeter.

and the particular challenges that arise from the perturbation operators of both valence and core-like character, of relevance to the present properties. As a technical note, the generated co2-MOR set, applied throughout the study features a less than 5% deviation from the basis-set limit for the V, V_{C}, and V_{H} constants.

The Verdet constant V parameterises the Faraday optical rotation (equation 2.23), and plays a similar role as the constant V_K for the NSOR phenomenon. Figures 4.10 and 4.11 illustrate the dispersion curves of these constants for the studied graphene and graphane molecules, respectively. The figures reveal a strong enhancement for both the FOR and NSOR phenomena in the vicinity of the optical excitation. The clearly diverging behaviour in these dispersion curves is partially due to the inadequacy of perturbation theory in close proximity of the excitation energies. However, the strong enhancement of the dispersion curves was recently observed also with a response technique that is convergent at resonances [44]. There are striking differences between these sp^2- and sp^3-hybridised systems. In the case of FOR at a given wavelength, V is about an order of magnitude larger in G than in the corresponding HG systems. For the G systems, the dispersion curves of V are redshifted with increasing system size, while such a shift hardly occurs at all for the HG systems. These differences arise most importantly from the delocalised character of the electronic structure of the G systems, including their decreasing excitation energies with the system size.

The dependence of FOR on the degree of partial hydrogenation was studied for the system size G4, by varying individually the hybridisation of its concentric rings, demonstrated in Figure 4.12. All these mixed systems possess individual dispersion curves; The characteristic redshift of the location of the onset of strongest dispersion again follows the decrease of the excitation energies of the systems.

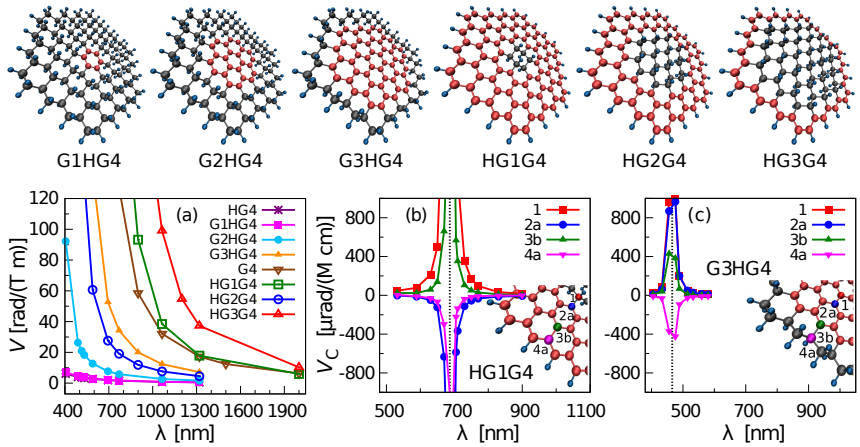

Figure 4.12. Atomic structures of the systems with different levels of partial hydrogenation, *i.e.*, mixed sp^2/sp^3-systems, in the size G4, and their different (a) isotropic Verdet constants (V). In panels (b) and (c), the isotropic NSOR constants V_C [10^{-6} rad/(M cm)] for the four nuclei from the centre to the perimeter in HG1G4 and G3HG4 systems are shown, respectively. Moreover, in (b) and (c), the strong excitation to singlet excited state with the transition dipole moment in the direction of the molecular plane (with large oscillator strength) is indicated with a dashed vertical line. The sp^2-hybridised carbon atoms are marked with red.

The study of the two different types of edge structure reveals that FOR is incapable of distinguishing between the zigzag and armchair perimeters. It appears that the dispersion curves of V, their form and magnitude, are determined solely by the excitation energy. This is due to the global character of the orbital Zeeman operator (3.24) by which the molecular wavefunction is coupled to the magnetic field. In contrast, in NSOR the optical activity is caused by the magnetisation of polarised nuclear spins. NSOR was found in Paper IV to have the potential to distinguish between the two different perimeters, Figure 4.13. This is due to the nucleus-specific resolution of NSOR that arises from the involved PSO hyperfine operator (3.25). This interaction is proportional to the inverse cube of the distance between the electron and the nucleus. Hence, NSOR probes the electronic structure locally, similarly to the nuclear shielding in conventional NMR.

The NSOR results in Figures 4.10 and 4.11 are represented as the dispersion curves of V_C for the innermost carbon nuclei with opposite directions of rotation, for G and HG, exemplifying the sensitivity of NSOR for the electronic structure. The ^{13}C and ^{1}H NSOR constants (Figure 5 of Paper IV) of the HG systems are nearly independent of the system size. This because the excitation energies of these HG systems are very similar. In contrast, in the sp^2-hybridised G systems, the V_C curves are redshifted similarly as in the case of FOR.

In Figure 4.13 it is demonstrated that different V_C dispersion curves arise from the different nuclear positions. It is observed that, from the size G4 onward, the innermost nuclei of the zigzag perimeter graphene flakes start to have mutually similar V_C dispersion

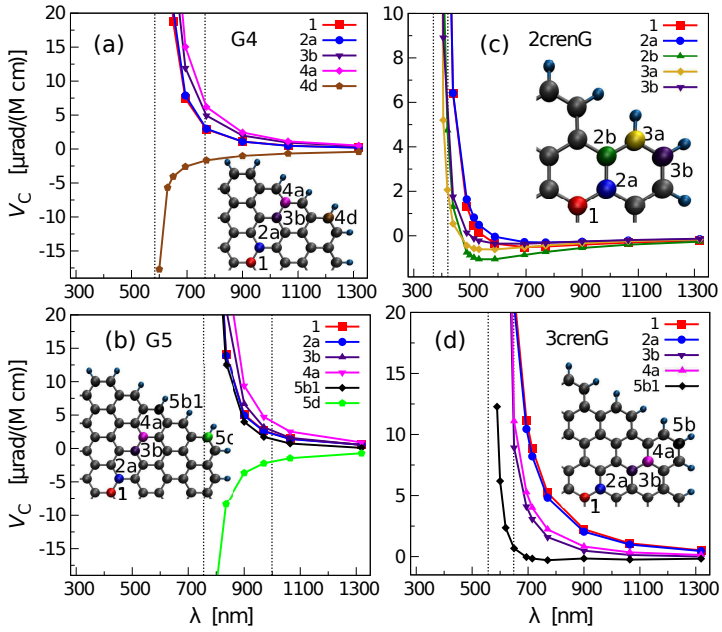

Figure 4.13. Nuclear spin optical rotation (NSOR) constants V_K for the largest studied graphene flakes. V_C [10^{-6} rad/(M cm)] for different nuclei in zigzag-perimeter systems: (a) G4, (b) G5, and armchair-perimeter systems: (c) 2crenG and (d) 3crenG. Two lowest excitation wavelengths to singlet excited states with the transition dipole moment in the direction of the molecular plane (with large oscillator strength) are indicated with dashed vertical lines.

curves, reflecting their identical electronic environment. Also noteworthy in these zigzag systems is the opposite sign of V_C for the apex nuclei, as compared to the NSOR constants resulting from the inner nuclei of G4 and G5 flakes. In the armchair-edged, 5crenG system, the curves of the inner nuclei fall into two distinguishable groups, instead. The clear difference between the perimeter types of these sp^2-systems is consistent with the fact that the cyclic sp^2-systems with zigzag boundaries (superbenzenes) have a relatively homogeneous graphene-like environment in the center region of the molecule, featuring delocalized π-electrons. Instead, the systems with full armchair perimeter possess more localised areas of π-electrons [136, 139, 142]. A corresponding behaviour is also seen in the ^{13}C chemical shift spectra of these systems, in Paper II.

Similarly to the case of the NMR spectra of HG systems (Paper II), V_C arising from the different nuclear positions of these systems, are notably different from each other only at the perimeter, as illustrated in Figures 7 and S12 of Paper IV. NSOR was also studied for two mixed sp^2/sp^3-systems at the model size G4. In these systems, named as G3HG4 and HG1G4, hydrogenation was applied either at the perimeter or at the center of the molecule, respectively. These two models have clearly different V_C curves, illustrated in Figure 4.12(bc). The largest sensitivity of NSOR is seen for the differently hybridised,

adjacent carbon nuclei. They feature opposite signs in their V_{C} dispersion curves, a feature observed for the mixed systems of both kinds.

To summarise, the present study demonstrates the characteristics of the Faraday rotation effects for finite graphene and graphane systems. What was found in the case of FOR was the independence of this property of the two studied perimeter types. In case of NSOR, the capability to sensitively characterise the local structure was clearly demonstrated. Paper IV should encourage experimentalists to both FOR measurements on graphene quantum dots, as well as to the eventual nuclear site-specific optical investigations of nuclear environments by NSOR, a field that is still at its very beginning.

5 Conclusions

The high abundance and versatile possibilities to form organic compounds of carbon constitute the basis of all known life. The tetravalent electronic structure of carbon enables many kinds of allotropes, exhibiting each possible dimensionality. Physical properties vary strongly between these forms. For instance, diamond is extremely hard and transparent, whereas graphite is soft and opaque [143]. Graphene is a sp^2-hybridised form of carbon with an extended honeycomb network, which enabled it to redefine the accessible limits of many material properties, $e.g.$, electric and thermal conductivity as well as mechanical strength. These and many other unusual properties have positioned graphene to a central role in nanoscience and -technology [4, 5]. The aim of the present work was to study the magnetic resonance and magneto-optic properties of different kinds of graphenes, including the pure, sp^2-hybridised graphene as well as the sp^3-hybridised graphane and fluorographene derivatives, both in their extended as well as finite-dimensional forms. This was motivated by the uncommon usage of magnetic resonance spectroscopies [18, 20, 27] in their structural characterisation. Additionally, we wanted to demonstrate the characterisation capability of spectroscopies based on magneto-optical rotation [43], which may provide a new way to study molecules and materials.

The theoretical framework for the work was provided by density-functional theory and specific perturbation techniques for the spectroscopic parameters. Throughout the work, the numerical quality of the computations was maintained as high as practically possible, to obtain parameters of predictive quality that may help in and encourage experimental work. Due to the different dimensionalities of the investigated systems, both molecular quantum chemistry and solid-state methods, were used. The properties involved and the size of the systems together constituted demanding computational challenges.

Magnetic resonance parameters for graphenes were investigated in Papers I-III. Paper I concerned the NMR parameters for G, HG and FG systems both in the bulk and at the limit of large finite systems. The limiting values were obtained by extrapolating the NMR properties of the innermost part of increasing-size graphene flakes, which converged to situation representative of large 2D graphene crystallites. The converged results in the case of finite band-gap HG and FG materials were compared to the obtained solid-state chemical shifts. The predictions of chemical shifts in these three types of environment throw light on the potential of NMR in the structural characterisation of these materials. Their spin-spin couplings, as well as the deuterium quadrupole coupling in HG, were also

calculated. Small 0D graphene flakes share many similarities with the 2D graphene but have also unique properties depending on the flake size and perimeter structure [11, 12]. Paper II focused on investigating the characteristic ^{13}C chemical shift spectral patterns of the finite flakes; the role of the size, composition and perimeter type. The findings in the qualitative spectral trends can help to understand and interpret experimental spectra that certainly will have a plethora of peaks [104]. It was observed that the innermost carbon sites of the sp^2-hybridised graphene flakes have a tendency to move towards smaller chemical shift values when the system size increases. In the case of the largest inspected graphene flakes, these interior nuclei produced a tightly-packed band of peaks. In contrast, the corresponding sites of sp^3-hybridised carbons in HG and FG fragments showed the opposite behaviour; they became less shielded with growing system size. In addition, the type of the perimeter structure caused in own specific characteristics. The main spectral behaviours were rationalised qualitatively by an analysis of the coupling of the electronic ground state of the systems to the excited states that are relevant for the NMR shielding tensor.

A particularly important verification of carbon-based magnetism was reported in Ref. [26], where spin-1/2 paramagnetism was observed in a graphene sample containing fluorine adatoms. ESR and pNMR spectroscopies are widely used for obtaining information of paramagnetic defects. Their capability to obtain structural information is demonstrated in Paper III. Therein, we predicted the ESR g- and $\mathbf{A}$-tensors, as well as the pNMR shielding constants and anisotropies for 2D graphenes with increasing separation of spin-1/2 point-defects. A remarkably high, local enhancement in the values of hyperfine coupling as well as pNMR shielding constants was observed in the vacancy-defected HG and FG systems. The defects created by hydrogen and fluorine adatoms in the sp^2-hybridised graphene also showed an enhancement in their corresponding parameters. Due to the delocalised electron structure, these parameters have a long-range character in these narrow band-gap systems. The g-tensor as a second-order property requires an energy gap, and, hence, failed to converge in these adatom-defected systems. In contrast, the vacancy-defected systems have finite band gaps and for them well-defined g-values can be obtained.

Being the thinnest and transparent conductive material, graphene has recently fascinated also with its unusually high Faraday rotation capability [133]. In Paper IV, we demonstrated the FOR properties of graphene flakes, focusing on the dependence on the size, perimeter structure and the level of hydrogenation of the systems. In addition, we studied the capability of the NSOR technique for nuclear site-specific optical investigations of these flakes. FOR occurs in the visible range in the finite graphene flakes, while the reported rotation of the 2D graphene was demonstrated to be in the infrared-range. We observed that FOR is similar for the zigzag- and armchair-edged graphene fragments, but it is greatly enhanced in the vicinity of the optical excitation energies of these flakes. These energies decrease for the G systems with their size and, therefore, the differently sized graphene systems have strong dispersion of the Verdet constant at different positions in the spectrum. Furthermore, FOR was observed to be sensitive to the degree of partial sp^2-hybridisation, which was inspected in differently hydrogenated, mixed sp^3/sp^2-hybridised flakes. In the case of NSOR, we observed clearly different dispersion curves of the NSOR constants for differently edged sp^2-hybridised flakes. Moreover we observed that, in the HG flakes, the nuclei caused the optical rotation to occur to the opposite direction, resulting in oppositely signed NSOR constants, than in the sp^2-hybridised flakes.

These studies of graphene systems support the potential of the magnetic and magneto-optic spectroscopic methods to be used in their characterisation. The sensitivity of the spectral parameters was demonstrated, giving insight to the electronic and atomic structure of these systems. In that regard the aims of the work have been fulfilled. The predictions should encourage experimental investigations also in other topical graphene derivatives [10] and carbon allotropes [144, 145].

References

[1] L. Landau, Physikalische Zeitschrift der Sowjetunion **1**, 26 (1937).

[2] P. R. Wallace, Phys. Rev. **71**, 622 (1947).

[3] A. K. Geim and K. S. Novoselov, Nature Mater. **6**, 183 (2007).

[4] A. K. Geim, Science **324**, 1530 (2009).

[5] L. E. F. Foa Torres, S. Roche, and J.-C. Charlier, *Introduction to Graphene-Based Nanomaterials: From Electronic Structure to Quantum Transport*, Cambridge University Press, New York, 2014.

[6] K. S. Novoselov, A. K. Geim, S. V. Morozov, D. Jiang, Y. Zhang, S. V. Dubonos, I. V. Grigorieva, and A. A. Firsov, Science **306**, 666 (2004).

[7] D. C. Elias, R. R. Nair, T. M. G. Mohiuddin, S. V. Morozov, P. Blake, M. P. Halsall, A. C. Ferrari, D. W. Boukhvalov, M. I. Katsnelson, A. K. Geim, and K. S. Novoselov, Science **323**, 610 (2009).

[8] R. R. Nair, W. Ren, R. Jalil, I. Riaz, V. G. Kravets, L. Britnell, P. Blake, F. Schedin, A. S. Mayorov, S. Yuan, M. I. Katsnelson, H.-M. Cheng, W. Strupinski, L. G. Bulusheva, A. V. Okotrub, I. V. Grigorieva, A. N. Grigorenko, K. S. Novoselov, and A. K. Geim, Small **6**, 2877 (2010).

[9] R. Zbořil, F. Karlický, A. B. Bourlinos, T. A. Steriotis, A. K. Stubos, V. Georgakilas, K. Šafářová, D. Jančík, C. Trapalis, and M. Otyepka, Small **6**, 2885 (2010).

[10] F. Karlický, K. Kumara Ramanatha Datta, M. Otyepka, and R. Zbořil, ACS Nano **7**, 6434 (2013).

[11] J. Wu, W. Pisula, and K. Müllen, Chem, Rev. **107**, 718 (2007).

[12] R. Rieger and K. Müllen, J. Phys. Org. Chem. **23**, 315 (2010).

[13] S. K. Hämäläinen, Z. Sun, M. P. Boneschanscher, A. Uppstu, M. Ijäs, A. Harju, D. Vanmaekelbergh, and P. Liljeroth, Phys. Rev. Lett. **107**, 236803 (2011).

[14] J. Shen, Y. Zhu, X. Yang, and C. Li, Chem. Commun. **48**, 3686 (2012).

[15] P. W. Atkins and J. de Paula, *Atkins' Physical Chemistry*, Oxford University Press, New York, 7^{th} edition, 2002.

[16] A. Abragam, *The Principles of Nuclear Magnetism*, Oxford University Press, Oxford, 1961.

[17] C. P. Slichter, *Principles of Magnetic Resonance*, Springer, Berlin, 2^{nd} edition, 1990.

[18] J. E. Harriman, *Theoretical Foundations of Electron Spin Resonance*, Academic, New York, 1978.

[19] J. Weil, J. Bolton, and J. Welz, *Electron Paramagnetic Resonance: Elementary Theory and Practical Applications*, Wiley, New York, 1994.

[20] J. Bertini, C. Luchinat, and G. Parigi, *Solution NMR of Paramagnetic Molecules*, Elsevier, Amsterdam, 2001.

[21] J. Vaara, Chemical shift in paramagnetic systems, in *High Resolution NMR Spectroscopy: Understanding Molecules and Their Electronic Structures*, edited by R. H. Contreras, volume 3 of *Science and Technology of Atomic, Molecular, Condensed Matter & Biological Systems*, pages 41–67, Elsevier, 2013.

[22] L. D. Barron, *Molecular Light Scattering and Optical Activity*, Cambridge University Press, Cambridge, 2009.

[23] A. Rizzo and S. Coriani, Birefringences: A challenge for both theory and experiment, in *Response Theory and Molecular Properties (A Tribute to Jan Linderberg and Poul Jørgensen)*, edited by H. J. A. Jensen, volume 50 of *Advances in Quantum Chemistry*, pages 143 – 184, Academic Press, 2005.

[24] I. M. Savukov, S.-K. Lee, and M. V. Romalis, Nature **442**, 1021 (2006).

[25] S. Ikäläinen, M. V. Romalis, P. Lantto, and J. Vaara, Phys. Rev. Lett. **105**, 153001 (2010).

[26] R. R. Nair, M. Sepioni, I.-L. Tsai, O. Lehtinen, J. Keinonen, A. V. Krasheninnikov, T. Thomson, A. K. Geim, and I. V. Grigorieva, Nature Phys. **8**, 199 (2012).

[27] M. H. Levitt, *Spin Dynamics Basics of Nuclear Magnetic Resonance*, Wiley, Chichester, 2001.

[28] T. Helgaker, M. Jaszuński, and K. Ruud, Chem. Rev. **99**, 293 (1999).

[29] H. D. Young, R. A. Freedman, and A. L. Ford, *University Physics with Modern Physics*, Addison-Wesley, Essex, 13^{th} edition, 2012.

[30] M. J. Duer, *Introduction to Solid-State NMR spectroscopy*, Blakwell Publishing Ltd, Oxford, 2014.

[31] P. W. Atkins and R. S. Friedman, *Molecular Quantum Mechanics*, Oxford University Press, New York, 5^{th} edition, 2011.

[32] T. Helgaker, S. Coriani, P. Jørgensen, K. Kristensen, J. Olsen, and K. Ruud, Chem. Rev. **112**, 543 (2012).

[33] National Institute of Standards and Technology.
CODATA, http://physics.nist.gov/cuu/Constants/index.html.

[34] Z. Rinkevicius, J. Vaara, L. Telyatnyk, and O. Vahtras, J. Chem. Phys. **118** (2003).

[35] S. Moon and S. Patchkovskii, First-principles calculations of paramagnetic nmr shifts, in *Calculation of NMR and EPR Parameters: Theory and Applications*, edited by M. Kaupp, M. Bühl, and V. G. Malkin, pages 325–338, Wiley, 2004.

[36] T. O. Pennanen and J. Vaara, J. Chem. Phys. **123**, 174102 (2005).

[37] M. Kaupp and F. H. Köhler, Coord. Chem. Rev. **253**, 2376 (2009).

[38] T. O. Pennanen and J. Vaara, Phys. Rev. Lett. **100**, 133002 (2008).

[39] E. Hecht, *Optics*, Addison-Wesley, Essex, 4^{th} edition, 2001.

[40] A. D. Buckingham and P. J. Stephens, Ann. Rev. Phys. Chem. **17**, 399 (1966).

[41] A. D. Buckingham and D. A. Long, Phil. Trans. R. Soc. A **293**, 239 (1979).

[42] T.-t. Lu, M. He, D.-m. Chen, T.-j. He, and F.-c. Liu, Chem. Phys. Lett. **479**, 14 (2009).

[43] J. Shi, S. Ikäläinen, J. Vaara, and M. V. Romalis, J. Phys. Chem. Lett. **4**, 437 (2013).

[44] J. Vaara, A. Rizzo, J. Kauczor, P. Norman, and S. Coriani, J. Chem. Phys. **140**, 134103 (2014).

[45] A. Leach, *Molecular Modelling: Principles and Applications*, Pearson Education Ltd., Essex, 2^{nd} edition, 1999.

[46] M. Born and R. Oppenheimer, Ann. Phys. **389**, 457 (1927).

[47] T. Helgaker, P. Jørgensen, and J. Olsen, *Molecular Electronic-Structure Theory*, John Wiley Sons, Ltd., West Sussex, 2004.

[48] D. R. Hartree, Proc. Cambr. Phil. Soc. **24**, 328 (1928).

[49] V. A. Fock, Z. Phys. **15**, 126 (1930).

[50] C. J. Cramer, *Essentials of Computatioal Chemistry*, John Wiley & Sons, Ltd, West Sussex, 2003.

[51] R. G. Parr and W. Yang, *Density-Functional Theory of Atoms and Molecules*, Oxford University Press, Oxford, 1989.

[52] S. Kümmel and J. P. Perdew, Phys. Rev. B **68**, 035103 (2003).

[53] F. Della Sala and A. Görling, J. Chem. Phys. **115** (2001).

[54] C. J. Cramer and D. G. Truhlar, Phys. Chem. Chem. Phys. **11**, 10757 (2009).

[55] W. Kohn and L. J. Sham, Phys. Rev. **140**, A1133 (1965).

[56] M. C. Payne, M. P. Teter, D. C. Allan, T. A. Arias, and J. D. Joannopoulos, Rev. Mod. Phys. **64**, 1045 (1992).

[57] D. J. Tozer, Density functional theory: the exchange-correlation energy, in *European Summerschool in Quantum Chemistry 2011, Book II*, edited by P.-O. Widmark, page 473, Department of Theoretical Chemistry Chemical Centre, 7^{th} edition, 2011.

[58] F. Neese, Coord. Chem. Rev. **253**, 526 (2009).

[59] J. P. Perdew, A. Ruzsinszky, J. Tao, V. N. Staroverov, G. E. Scuseria, and G. I. Csonka, J. Chem. Phys. **123**, (2005).

[60] J. P. Perdew, K. Burke, and M. Ernzerhof, Phys. Rev. Lett., **77**, 3865 (1996); Phys. Rev. Lett., **78**, 1396 (1997) (erratum).

[61] J. R. Yates and C. J. Pickard, Computations of magnetic resonance parameters for crystalline systems: Principles, in *Encyclopedia of Magnetic Resonance*, edited by R. K. Harris, John Wiley & Sons, Ltd, 2007.

[62] C. Lee, W. Yang, and R. G. Parr, Phys. Rev. B. **37**, 785 (1988).

[63] A. D. Becke, Phys. Rev. A. **38**, 3098 (1988).

[64] A. D. Becke, J. Chem. Phys. **98**, 5648 (1993).

[65] P. J. Stephens, F. J. Devlin, C. F. Chabalowski, and M. J. Frisch, J. Phys. Chem. **98**, 11623 (1994).

[66] C. C. J. Roothaan, Rev. Mod. Phys. **23**, 69 (1951).

[67] G. G. Hall, Proc. R. Soc. Lond. A **205**, 541 (1951).

[68] S. F. Boys, Proc. Roy. Soc. A **200**, 542 (1950).

[69] S. P. A. Sauer, *Molecular Electromagnetism*, Oxford University Press, New York, 2011.

[70] P. Manninen and J. Vaara, J. Comput. Chem. **27**, 434 (2006).

[71] F. Weigend and R. Ahlrichs, Phys. Chem. Chem. Phys. **7**, 3297 (2005).

[72] N. W. Ashcroft and D. Mermin, *Solid State Physics*, Saunders College, Philadelphia, 1976.

[73] M. Methfessel and A. T. Paxton, Phys. Rev. B **40**, 3616 (1989).

[74] N. Marzari, D. Vanderbilt, A. De Vita, and M. C. Payne, Phys. Rev. Lett. **82**, 3296 (1999).

[75] H. J. Monkhorst and J. D. Pack, Phys. Rev. B **13**, 5188 (1976).

[76] P. Giannozzi et al., J. Phys.: Condens. Matter **21**, 395502 (2009).

[77] R. Dovesi, R. Orlando, A. Erba, C. M. Zicovich-Wilson, B. Civalleri, S. Casassa, L. Maschio, M. Ferrabone, M. De La Pierre, P. D'Arco, Y. Noël, M. Causà, M. Rérat, and B. Kirtman, Int. J. Quantum Chem. **114**, 1287 (2014).

[78] J. M. Soler, E. Artacho, J. D. Gale, A. García, J. Junquera, P. Ordejón, and D. Sánchez-Portal, J. Phys: Condens. Matter **14**, 2745 (2002).

[79] J. C. Phillips, Phys. Rev. **112**, 685 (1958).

[80] P. E. Blöchl, Phys. Rev. B **50**, 17953 (1994).

[81] K. G. Dyall and K. J. Fægri, *Introduction to Relativistic Quantum Chemistry*, Oxford University Press, New York, 2007.

[82] K. Wolinski, J. F. Hinton, and P. Pulay, J. Am. Chem. Soc. **112**, 8251 (1990).

[83] T. Helgaker and P. Jørgensen, J. Chem. Phys. **95**, 2595 (1991).

[84] S. Baroni, P. Giannozzi, and A. Testa, Phys. Rev. Lett. **58**, 1861 (1987).

[85] C. J. Pickard and F. Mauri, Phys. Rev. B **63**, 245101 (2001).

[86] J. Olsen and P. Jørgensen, J. Chem. Phys. **82**, 3235 (1985).

[87] A. Rizzo, S. Coriani, and K. Ruud, Response function theory computational approaches to linear and nonlinear optical spectroscopy, in *Computational Strategies for Spectroscopy*, edited by J. Barone, pages 77–135, John Wiley & Sons, 2011.

[88] L. Truflandier, M. Paris, and F. Boucher, Phys. Rev. B **76**, 035102 (2007).

[89] N. F. Ramsey, Phys. Rev. **78**, 695 (1950).

[90] N. F. Ramsey, Phys. Rev. **91**, 303 (1953).

[91] J. Vaara, Phys. Chem. Chem. Phys. **9**, 5399 (2007).

[92] T. Gregor, F. Mauri, and R. Car, J. Chem. Phys. **111**, 1815 (1999).

[93] T. Charpentier, Solid State Nucl. Magn. Res. **40**, 1 (2011).

[94] W. E. Lamb, Phys. Rev. **60**, 817 (1941).

[95] M. Profeta, F. Mauri, and C. J. Pickard, J. Am. Chem. Soc. **125**, 541 (2003).

[96] C. J. Pickard and F. Mauri, Phys. Rev. Lett. **88**, 086403 (2002).

[97] C. G. Van de Walle and P. E. Blöchl, Phys. Rev. B **47**, 4244 (1993).

[98] P. E. Blöchl, Phys. Rev. B **62**, 6158 (2000).

[99] O. V. Yazyev, I. Tavernelli, L. Helm, and U. Röthlisberger, Phys. Rev. B **71**, 115110 (2005).

[100] M. S. Bahramy, M. H. F. Sluiter, and Y. Kawazoe, Phys. Rev. B **76**, 035124 (2007).

[101] M. Jaszuński and A. Rizzo, Mol. Phys. **96**, 855 (1999).

[102] M. J. Allen, V. C. Tung, and R. B. Kaner, Chem. Rev. **110**, 132 (2010).

[103] K. S. Novoselov, V. I. Fal'ko, L. Colombo, P. R. Gellert, M. G. Schwab, and K. Kim, Nature **490**, 192 (2012).

[104] C. D. Simpson, J. D. Brand, A. J. Berresheim, L. Przybilla, H. J. Rader, and K. Müllen, Chem. Eur. J. **8**, 1424 (2002).

[105] S. Thongrattanasiri, A. Manjavacas, and F. J. García de Abajo, ACS Nano **6**, 1766 (2012).

[106] A. Manjavacas, F. Marchesin, S. Thongrattanasiri, P. Koval, P. Nordlander, D. Sánchez-Portal, and F. J. García de Abajo, ACS Nano **7**, 3635 (2013).

[107] S. Bernadotte, F. Evers, and C. R. Jacob, J. Phys. Chem. C **117**, 1863 (2013).

[108] D. B. Chesnut and K. D. Moore, J. Comput. Chem. **10**, 648 (1989).

[109] J. Kaski, P. Lantto, J. Vaara, and J. Jokisaari, J. Am. Chem. Soc. **120**, 3993 (1998).

[110] Y. Si and E. T. Samulski, Nano Letters **8**, 1679 (2008).

[111] W. Gao, L. B. Alemany, L. Ci, and P. M. Ajayan, Nature Chem. **1**, 403 (2009).

[112] D. C. Marcano, D. V. Kosynkin, J. M. Berlin, A. Sinitskii, Z. Sun, A. Slesarev, L. B. Alemany, W. Lu, and J. M. Tour, ACS Nano **4**, 4806 (2010).

[113] A. M. Panich, A. I. Shames, A. E. Aleksenskii, and A. Dideikin, Solid State Commun. **152**, 466 (2012).

[114] A. Panich, Synt. Met. **100**, 169 (1999).

[115] K. Guérin, J. P. Pinheiro, M. Dubois, Z. Fawal, F. Masin, R. Yazami, and A. Hamwi, Chem. Mater. **16**, 1786 (2004).

[116] P. Lantto, J. Kaski, J. Vaara, and J. Jokisaari, Chem. Eur. J. **6**, 1395 (2000).

[117] O. V. Yazyev, Rep. Prog. Phys. **73**, 056501 (2010).

[118] F. Banhart, J. Kotakoski, and A. V. Krasheninnikov, ACS Nano **5**, 26 (2011).

[119] O. V. Yazyev and L. Helm, Phys. Rev. B **75**, 125408 (2007).

[120] D. W. Boukhvalov, M. I. Katsnelson, and A. I. Lichtenstein, Phys. Rev. B **77**, 035427 (2008).

[121] H. Şahin, C. Ataca, and S. Ciraci, Phys. Rev. B **81**, 205417 (2010).

[122] H. Şahin, M. Topsakal, and S. Ciraci, Phys. Rev. B **83**, 115432 (2011).

[123] J. O. Sofo, A. M. Suarez, G. Usaj, P. S. Cornaglia, A. D. Hernández-Nieves, and C. A. Balseiro, Phys. Rev. B **83**, 081411 (2011).

[124] J. O. Sofo, G. Usaj, P. S. Cornaglia, A. M. Suarez, A. D. Hernández-Nieves, and C. A. Balseiro, Phys. Rev. B **85**, 115405 (2012).

[125] H. Y. Liu, Z. F. Hou, C. H. Hu, Y. Yang, and Z. Z. Zhu, J. Phys. Chem. C **116**, 18193 (2012).

[126] E. J. G. Santos, A. Ayuela, and D. Sánchez-Portal, New J. Phys. **14**, 043022 (2012).

[127] M. Sepioni, R. R. Nair, S. Rablen, J. Narayanan, F. Tuna, R. Winpenny, A. K. Geim, and I. V. Grigorieva, Phys. Rev. Lett. **105**, 207205 (2010).

[128] X. Hong, S.-H. Cheng, C. Herding, and J. Zhu, Phys. Rev. B **83**, 085410 (2011).

[129] K. M. McCreary, A. G. Swartz, W. Han, J. Fabian, and R. K. Kawakami, Phys. Rev. Lett. **109**, 186604 (2012).

[130] X. Hong, K. Zou, B. Wang, S.-H. Cheng, and J. Zhu, Phys. Rev. Lett. **108**, 226602 (2012).

[131] A. Y. S. Eng, H. L. Poh, F. Šaněk, M. Maryško, S. Matějková, Z. Sofer, and M. Pumera, ACS Nano **7**, 5930 (2013).

[132] P. Sun, K. Wang, J. Wei, M. Zhong, D. Wu, and H. Zhu, Nano Res. **7**, 1507 (2014).

[133] I. Crassee, J. Levallois, A. L. Walter, M. Ostler, A. Bostwick, E. Rotenberg, T. Seyller, D. van der Marel, and A. B. Kuzmenko, Nature Phys. **7**, 48 (2011).

[134] A. Manjavacas, P. Nordlander, and F. J. García de Abajo, ACS Nano **6**, 1724 (2012).

[135] Z. Fang, S. Thongrattanasiri, A. Schlather, Z. Liu, L. Ma, Y. Wang, P. M. Ajayan, P. Nordlander, N. J. Halas, and F. J. García de Abajo, ACS Nano **7**, 2388 (2013).

[136] S. E. Stein and R. L. Brown, J. Am. Chem. Soc. **109**, 3721 (1987).

[137] K. Nakada, M. Fujita, G. Dresselhaus, and M. S. Dresselhaus, Phys. Rev. B **54**, 17954 (1996).

[138] M. R. Philpott and Y. Kawazoe, J. Chem. Phys. **131**, 214706 (2009).

[139] M. R. Philpott and Y. Kawazoe, Chem. Phys. **358**, 85 (2009).

[140] S. Ikäläinen, P. Lantto, P. Manninen, and J. Vaara, J. Chem. Phys. **129**, 124102 (2008).

[141] P. Štěpánek, M. Straka, V. Andrushchenko, and P. Bouř, J. Chem. Phys. **138**, 151103 (2013).

[142] K. Sakamoto, N. Nishina, T. Enoki, and J.-i. Aihara, J. Phys. Chem. A **118**, 3014 (2014).

[143] J. Clayden, N. Greeves, S. Warren, and P. Wothers, *Organic Chemistry*, Oxford University Press, New York, 2001.

[144] J.-T. Wang, C. Chen, E. Wang, and Y. Kawazoe, Sci. Rep. **4** (2014).

[145] B. R. Sharma, A. Manjanath, and A. K. Singh, Sci. Rep. **4** (2014).

Original papers

I Reproduced with permission from Physical Chemistry Chemical Physics.
J. Vähäkangas, S. Ikäläinen, P. Lantto, and J. Vaara,
Nuclear Magnetic Resonance Predictions for Graphenes: Concentric Finite Models and Extrapolation to Large Systems. **15**, 4634−4641, (2013).

II Reproduced with permission from ChemPhysChem.
N. Özcan, J. Vähäkangas, P. Lantto, and J. Vaara,
Characteristic spectral patterns in the ^{13}C nuclear magnetic resonance of hexagonal and crenellated graphene fragments. **15**, 1799−1808, (2014).

III Manuscript submitted for publication
J. Vähäkangas, P. Lantto, J. Mareš, and J. Vaara,
Spin Doublet Point Defects in Graphenes: Predictions for ESR and pNMR Spectral Parameters.

IV Reproduced with permission from Physical Chemistry C.
J. Vähäkangas, P. Lantto, and J. Vaara,
Faraday rotation in graphene quantum dots: Interplay of size, perimeter type and functionalization. **118**, 23996−24005, (2014).